EES Catalysis

REVIEW ARTICLE

View Article Online
View Journal | View Issue

Cite this: *EES Catal.*, 2023, 1, 619

Strategies for the design of ruthenium-based electrocatalysts toward acidic oxygen evolution reaction

Liqiang Hou,[a] Xiumin Gu,[a] Xuemei Cui,[a] Jiachen Tang,[a] Zijian Li,[b] Xien Liu *[a] and Jaephil Cho *[c]

Polymer electrolyte membrane water electrolyzers (PEMWEs) driven by renewable electricity are deemed to be a promising technology toward green hydrogen production, where anodic oxygen evolution reaction (OER) is one of the main obstacles that impede the practical application of PEMWEs. The strongly acidic environment and greatly oxidative working conditions make the development of highly active and stable electrocatalysts toward OER extremely challenging. Ruthenium (Ru)-based materials as acidic OER catalysts possess a number of advantages including high activity and the lowest price among the precious metal family, while their long-term durability is far from satisfactory. To date, effective efforts have been made to improve the durability of Ru species to balance activity and stability. In this review, the recent progress in the development of Ru-based catalysts for enhanced acidic OER performance is summarized, expecting to offer guidance for exploring highly active and stable Ru-based catalysts. The fundamental understanding of the relationship between OER mechanism and activity as well as stability of Ru species is discussed. Then, experimental attempts to improve the acidic OER performance of Ru-based catalysts are reviewed. Finally, the challenges and perspectives for future studies of Ru-based catalysts for acidic OER are also proposed.

Received 27th April 2023,
Accepted 7th June 2023

DOI: 10.1039/d3ey00092c

rsc.li/eescatalysis

Broader context

Polymer electrolyte membrane water electrolyzers (PEMWEs) have been deemed to be one of the promising techniques to produce renewable hydrogen. The strong corrosive condition and high operating potential lead to serious challenges for the development of significantly active and durable catalysts toward anodic oxygen evolution reaction (OER). Catalysts based on ruthenium (Ru), which is the cheapest noble metal, can deliver high activity for the acidic OER. Nevertheless, the lack of reasonable durability of Ru-based catalysts for acidic OER prevents them from further large-scale applications. Within this scenario, a comprehensive discussion of the fundamental understanding of the relationship between OER mechanism and activity as well as stability of Ru-based catalysts is provided. Second, recent progress in the development of Ru-based catalysts for acidic OER is reviewed with an emphasis on the underlying structure–performance relationships. Last, the remaining challenges and personal perspectives for future studies on Ru-based OER catalysts are proposed to realize the commercialization of electrochemical water splitting.

1. Introduction

The excessive use of fossil fuels brings about not only resource exhaustion, but also severe environmental issues, such as the greenhouse effect, air contamination, and so on, which are badly in need of storage and conversion technologies for renewable energy.[1–4] Green hydrogen, continuously produced by electrochemical water splitting coupled with renewable electricity, is regarded as a potential energy carrier.[5–7] Alkaline water electrolyzer (AWE) technology was industrialized for the first time in the 1920s, and then gradually developed into a matured commercial application technology.[8,9] However, AWE is subject to high ohmic losses, low working pressure, slow kinetics, and low operating current density.[10] These shortcomings were not resolved until the proposal of the concept of solid polymer electrolytes by Grubb.[11] Polymer electrolyte membrane water electrolyzers (PEMWEs) can operate with a larger power input range due to the high proton conductivity and lower

[a] State Key Laboratory Base of Eco-Chemical Engineering, College of Chemical Engineering, Qingdao University of Science and Technology, Qingdao 266042, P. R. China. E-mail: liuxien@qust.edu.cn
[b] Department of Chemistry, City University of Hong Kong, Hong Kong SAR 999077, P. R. China
[c] Department of Energy Engineering, Department of Energy and Chemical Engineering, Ulsan National Institute of Science and Technology (UNIST), Ulsan 44919, South Korea. E-mail: jpcho@unist.ac.kr

hydrogen permeability of the membrane, which can ensure their high working current density and hydrogen purity.[8,12–15] Moreover, PEMWEs with a compact structure can provide working pressure as high as 350 bar, facilitating the delivery of compressed hydrogen.[16,17] However, the cosmically commercial PEMWEs are unfortunately hindered by the electrocatalytic property, especially stability, of anodic catalysts, attributed to the strongly acidic environment and the severe oxidative working conditions.[18–20]

Electrochemical water splitting consists of an anodic oxygen evolution reaction (OER) and a cathodic hydrogen evolution reaction (HER).[21–23] The cathodic HER is a two-electron reaction, and is one of the simplest electrochemical reactions and is relatively effortless to achieve. However, the anodic OER is a complex multi-step reaction and involves four-electron transfer, leading to a much higher energy expenditure to surmount the kinetic barrier than HER.[24,25] To date, substantial OER catalysts, including alloys, metal oxides, pyrochlores, and perovskites, have been developed to improve anodic electrode kinetics and stability.[26–28] However, on account of the thermodynamic unsteadiness of non-noble metal elements under harsh acidic OER operation conditions, the most promising acidic OER catalysts are restricted to precious metals at the present stage.[29] As forecasted by the theoretical volcano maps, ruthenium (Ru)-based and iridium (Ir)-based compounds are currently considered the most advanced OER catalysts under strong acidic environments.[4,30,31] Note that Ir-based oxides are the most promising candidates to reach the stability standard of PEMWE equipment, owing to their superior acid resistance and oxidation resistance.[32–34] Nevertheless, because of the extremely scarce feature of Ir, more than 40 years of global Ir production is required to scale up PEMWE to the terawatt-level.[35–37] As the cheapest member of the Pt-related precious metal family, more abundant Ru-based materials deliver relatively superior OER mass activities compared with Ir-related catalysts.[38,39] A variety of strategies, including surface engineering,[40,41] alloy engineering,[42,43] and single atom engineering,[44] have been exploited to construct advanced Ru-related OER catalysts. Satisfyingly, an extremely low overpotential of $\sim$150 mV at 10 mA cm^{-2} current density can be achieved under strong acidic electrolytes.[17,45] Unfortunately, the over-oxidation of RuO_2 to soluble RuO_4 species would inevitably occur under the highly oxidizing voltage and strong acidic medium,[46–48] which calls into question the durability of Ru-related catalysts and leaves the infinite possibility for improvement (Fig. 1).

To date, the dynamic dissolution process of Ru-related acidic OER catalysts has been extensively studied. More importantly, diverse *in situ*/operando means, including operando X-ray absorption spectroscopy (XAS),[49,50] *in situ* ATR-SEIRAS,[51,52] operando X-ray photoelectron spectroscopy (XPS),[53] *in situ* Raman,[54] and isotope labeling measurements,[55,56] have been adopted to explore the dissolution behavior of Ru-related derivatives during the acidic OER process. Moreover, theoretical calculations (DFT) have also been conducted to simulate the reaction behavior and process of Ru-related species during the acidic OER process.[57–60] These results not only confirm existing theories but also offer new insights into the durability of Ru-related OER catalysts in acidic electrolytes. Despite these achievements, available measures to increase the stability of Ru-related OER catalysts while maintaining their high activity are still relatively limited. Several excellent reviews on similar topics have been published in recent years,[26,38] while a comprehensive systematic review of engineering strategies for Ru-related acidic OER electrocatalysts and their corresponding

Liqiang Hou

Liqiang Hou received his PhD from China University of Petroleum in 2021. He is an associate professor at Qingdao University of Science & Technology. His scientific interest includes the design and synthesis of electrocatalysts for HER and OER.

Xien Liu

Xien Liu received his PhD from Dalian University of Technology in 2006. He is a professor at Qingdao University of Science & Technology. His research interest is mainly focused on electrocatalysts for OER, ORR, HER, CO_2 and N_2 reduction.

Jaephil Cho

Jaephil Cho is a distinguished professor at UNIST (Republic of Korea). He is a director of the Battery R & D Center at UNIST. His current research is focused mainly on Li-ion and all-solid-state Li-ion batteries.

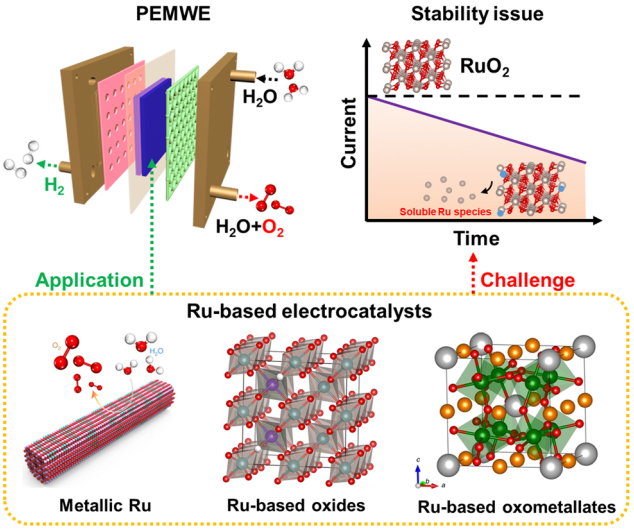

Fig. 1 Illustration of the stability challenge of Ru-based electrocatalysts for PEMWEs.

structural and electronic modulation effects is lacking and needed. Therefore, in this review, we would like to emphasize the theoretical and experimental studies of the basic relationship among structure–activity–stability and offer reasonable directions to construct advanced Ru-based catalysts for practical applications. We first discuss the relationship between OER mechanism and activity as well as stability of Ru-related acidic OER catalysts. Thereafter, recent representative efforts on improving the stability of Ru-based catalysts with high activity will also be comprehensively classified and discussed. In the end, we will outline some unresolved questions and provide some personal opinions toward future explorations of Ru-based OER catalysts.

2. Mechanistic studies on Ru-based OER electrocatalysts

Generally speaking, the overall electrocatalytic performances of Ru-based catalysts include activity and stability, which are closely related to the reaction mechanisms. To better analyze the relationship between reaction mechanisms and activity or stability, we summarize them separately.

2.1 The relationship between reaction mechanisms and activity

Analogous to other electrochemical reactions, the adsorption energy of reaction intermediates can also be applied to describe the OER activity.[18,61–64] In 2007, the oxygen adsorption energy (ΔG_{O^*}) was first applied to define the electrocatalytic activity of an OER catalyst by Rossmeisl *et al.*[61] They observed that the binding energy of the relevant OER intermediates on the surfaces of a catalyst (*i.e.*, OH*, O*, OOH*) follows a linear relationship. In other words, the binding energy fluctuation of one oxygen-related reaction intermediate could lead to the binding energy fluctuation of other oxygen-related reaction intermediates, which will inevitably impede optimizing the activity of a catalyst *via* only improving one reaction step. Fig. 2a shows the theoretical activity of OER as a linear function of the oxygen binding energy (O*), indicating optimal adsorption energy corresponding to the best OER activity and conforming to the above-discussed linear scaling relationship.[62] Rossmeisl *et al.* further identified the linear scaling relationship between the adsorption energy of HOO* and HO* with an approximately constant, which can in reverse define the lowest theoretical activity of an OER catalyst. As presented in Fig. 2b, the relationship between OER activity and the standard free energy of $\Delta G^0_{O^*} - \Delta G^0_{HO^*}$ presented a volcano tendency. As a result, the volcano map indicated that an excellent OER electrocatalyst should have moderate bonding energies with the oxygen-related reaction intermediates.

In spite of the restrictions of the linear scaling relationship on enhancing the activity of catalysts to reach the thermodynamic potential limitation of the OER, Halck *et al.* broke the linear correlation of the adsorption energies by embellishing the oxide surface.[65] Conventionally, the coordinatively unsaturated sites (cus) were considered as the active center for the OER. Nevertheless, they found that a dopant like Co or Ni atom located in the bridge site can activate the commonly inactive oxygen atom at the top as a proton donor or receiver, thus lowering the OER overpotential of RuO_2 (Fig. 2c).[15,65] According to theoretical analysis, the proton donor–acceptor functionality would not only function as a hydrogen acceptor from Ru–OH or Ru–OOH intermediates to reduce their energy state, but also not affect the reaction activity at the cus. More importantly, the additional parameter only influenced two of the three oxygen-related reaction intermediates, thus breaking the linear scaling relationship. Besides, Liu *et al.* found that the bridging O atom could serve as a proton-acceptor functionality even on pure RuO_2, and the H_2O tended to attack the aggregation of two surface O groups during the O–O bond formation stage (Fig. 2d and e).[66] Furthermore, Chen *et al.* proved that the electronic structures of bridging oxygen atom sites as proton receivers at the surface of RuO_2 played a significant role in the OER activity, which could be adjusted by the introduction of foreign metal atoms (Fig. 2f).[67] Therefore, these theoretical works have pointed out guidelines for the rational design of significantly active Ru-related OER catalysts.

In addition, note that catalytic descriptors are important means to analyze the relationship between catalytic behavior and the catalysts, which can also unscramble the activity tendency and find more highly active catalysts.[67–72] For example, the d-band theory has become a widely used tool to analyze and forecast the relationship between the electronic properties and activity of catalysts since it was proposed by Hammer and Nørskov.[71] Henceforward this theory has been extensively applied to describe bond formation on the surface of catalysts with the diverse filling of the d band. In terms of the interaction between adsorbates and the surface of catalysts, the coupling to a broad metal band will result in broadened and lowered electronic states of the adsorbate (Fig. 3a).[72] Generally

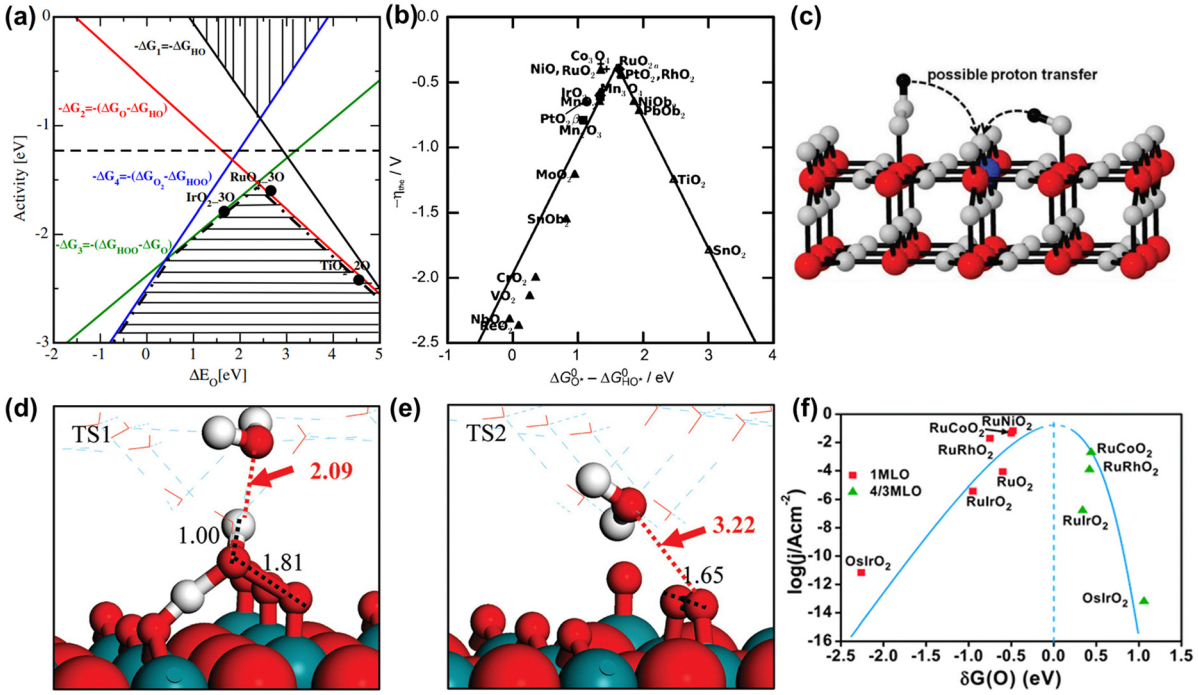

Fig. 2 (a) OER activity as a function of oxygen binding energy. (b) A volcano-type plot between OER activity and standard free energy change $\Delta G^0_{O^*} - \Delta G^0_{HO^*}$.[62] (c) Schematic illustration of the (110) surface of rutile RuO_2 modified by Ni doping.[15] (d and e) Transition state (TS) structures of water dissociation (TS1) and surface oxygen coupling (TS2) on the O-terminated phase of RuO_2(110).[66] (f) The calculated reaction rate of OER on different oxides as a function of δG(O).[67]

speaking, the farther the d states are away from the Fermi level, the higher energy is for the antibonding states and the stronger binding energy is between the adsorbate and the surface of catalysts. Moreover, the d-band center position could be adjusted by embellishing the electronic properties of catalysts *via* diverse ways (doping, alloying, strain engineering, *etc.*), which can realize the optimal interaction between adsorbates and catalysts to improve OER performance.[73–76] Yang *et al.* revealed that the distance between the d-band center and the Fermi level was larger than RuO_2 when Cu was doped into RuO_2. This result showed the lowered antibonding energy states and the weakened interaction between adsorbed O species and Ru (Fig. 3b).[76]

Later, the O 2p band center theory was also established. As shown in Fig. 3c, the d band broke up into two e_g states at the higher energy level while it broke up into three t_{2g} states at the lower energy level in the field of octahedral coordination.[77] There is a strong overlap between e_g doublets and O 2p orbitals, which will produce σ-bonding and σ*-antibonding states. However, there was a weak overlap between the t_{2g} triplets and the O 2_p orbital, which will generate π-bonds and π*-antibonds. Owing to the translational symmetry of the unit cell, the molecular orbitals turned into bands in oxide crystals, which were expressed as the metal d band and the O 2p band. The bonds formed from the hybridization of metal d bands and O 2p bands could be easily tuned by tuning the electronic properties of catalysts. Our group has investigated the function between OER activity and composition for $Cu_xRu_yO_{12}$ catalysts *via* the O 2p band center theory. It can be concluded by the theoretical study that when the O 2p bands were far away from the Fermi level in comparison to the Ru 4d bands, the lattice oxygen was greatly limited and the OER mechanism tended to the adsorbate evolution mechanism (AEM).[78] In contrast, when the O 2p band center got close to the Ru 4d orbital center, the lattice oxygen at the catalyst surface was more likely to take part in the reaction and the OER mechanism was inclined to the lattice oxygen evolution mechanism (LOM) (Fig. 3d). The obvious correlation between the computed relative OER overpotentials ($\eta^{LOM} - \eta^{AEM}$) and the difference value between O 2p and Ru 4d-band centers ($\varepsilon_{O\,2p} - \varepsilon_{Ru\,4d}$) indicated that the switching between the OER mechanism can be tuned by the amount of Cu or Ni (Fig. 3e).

Over the past decade, beyond d-band and O 2p center theories, extensive works have been done to establish catalytic descriptors to explore the optimal catalysts, including e_g orbital occupancy,[79] metal-oxygen covalency,[80] average O-2p-state energy,[62] coordinatively unsaturated metal cation,[81] and so on. What calls for special attention is that every above-mentioned descriptor has its limited application domain, and more new effective descriptors need to be established to analyze the Ru-related catalysts. Very recently, Ge *et al.* reported that the Ru charge was defined as a descriptor to describe the overall performance of Ru-related catalysts (Fig. 3f).[82] Moreover, they have managed to regulate the OER mechanism (AEM or LOM) and precisely control the activity and stability under the AEM by changing

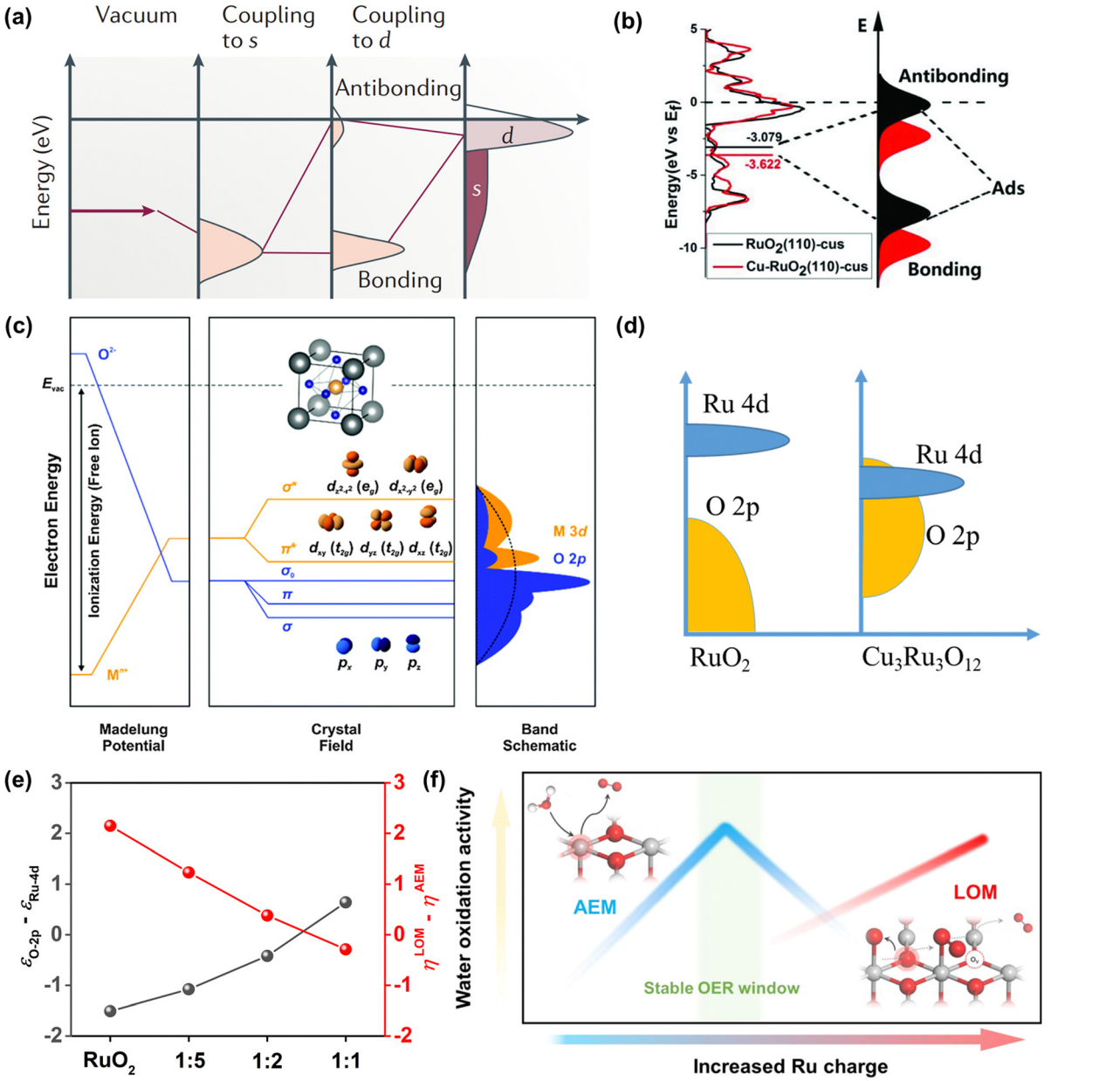

Fig. 3 (a) Schematic illustration of bond formation at a transition-metal surface. The lower the d states in energy relative to the EF, the more filled the antibonding states and the weaker the adsorption bond.[72] (b) The density of states plots of RuO_2 and Cu-RuO_2, and the corresponding schematic illustration of bond formation between the reaction surface and the adsorbate.[76] (c) Physical origin of shifts in constituent ion orbitals for oxides with octahedral oxygen coordination around transition metal ions. The dashed line represents the energy of free vacuum.[77] (d) An illustration of how the corresponding position of Ru 4d and O 2p orbitals regulates the reaction mechanism of OER on $Cu_xRu_yO_{12}$. (e) The computed relative OER overpotentials ($\eta^{LOM} - \eta^{AEM}$) *vs.* the value of $\varepsilon_{O\,2p} - \varepsilon_{Ru\,4d}$ for the four structural models.[78] (f) Schematic illustration of OER activity and stability of Ru-based catalysts within different reaction routes on the scale of Ru charge.[82]

the chelating atoms around the RuO6 species in $MRuO_x$ solid solution.

2.2 The relationship between reaction mechanism and stability

Ru-related materials are widely considered to be extremely unstable when acting as OER catalysts in a strongly acidic medium. During the same OER process, RuO_2 will dissolve severely under high overpotential owing to its serious overoxidation, while the dissolution rate of Ru is severalfold quicker than Ru-related oxides.[83,84] Over the years, extensive efforts have been made to grasp and understand the degradation mechanism of Ru-related catalysts in the OER, universally attributing to the generation of unstable RuO_4 species *via* the participation of lattice oxygen (Fig. 4a).[85] Moreover, the formation and exfoliation of RuO_4 species from the electrode can be quantitatively detected by using inductively coupled plasma-mass spectrometry; meanwhile, the presence of ruthenium oxy

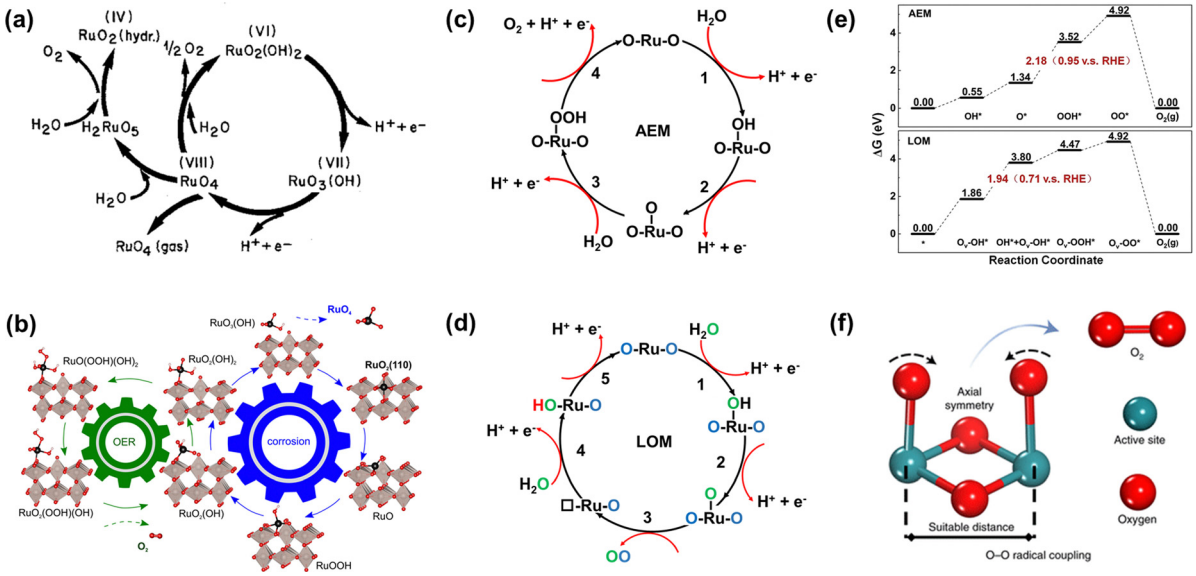

Fig. 4 (a) Model for the oxygen evolution and corrosion on Ru and RuO_2 electrodes.[85] (b) Schematic representation of the found coupling between corrosion and oxygen evolution reaction for the RuO_2(110) surface.[87] (c) The adsorbate evolution mechanism (AEM). (d) The lattice oxygen evolution mechanism (LOM). (e) The free energy diagrams of the two mechanisms of LOM and AEM for Co-doped RuO_2.[97] (f) O–O radical coupling promoted by symmetric dual active sites.[99]

species in the electrolyte can also be identified by using *in situ* reflection spectroscopy.[86] In addition, Klyukin *et al.* revealed that the launch of OER and dissolution occurred synchronously for RuO_2, suggesting that the dissolution was caused by OER (Fig. 4b).[87] It is worth noting that though the dissolved RuO_4 species can be relieved *via* redeposition in the reaction process as presented in Fig. 4a, the durability of Ru-based catalysts would be still greatly deteriorated.

Furthermore, the durability of Ru-related catalysts is closely related to the OER mechanisms.[15,88,89] Over the years, different OER mechanisms in acidic electrolytes have been proposed to uncover the OER process, which is aimed to offer directions for the construction of advanced OER catalysts. Generally, the two most credible hypotheses are known as AEM and LOM in accordance with the origin of the produced O_2 molecule.[90–92] For the AEM in acidic media, all the oxygen atoms in the produced O_2 molecules are derived from the adsorbed water, and such an OER process is made up of four synchronous proton–electron transfer procedures as presented in Fig. 4c. In terms of the LOM, it involves the surface lattice oxygen redox. That is, the excited lattice oxygen atoms in catalysts will take part in the water oxidation steps, and finally the oxygen atoms in the generated O_2 derive from both adsorbed water and the lattice of Ru-based catalysts as shown in Fig. 4d. Excitingly, the formation of the O═O bond is not accompanied by the generation of Ru–OOH, and therefore breaks the scaling relationships.[62,93,94] Significantly, the surface of Ru-related catalysts *via* the AEM process is deemed to be stable with only valence variation of the active sites, while the surface is unstable through the LOM process with the generation of activated lattice oxygen.[95] This result is due to the rate of oxygen vacancy (O_v) formation being generally faster than that of O_v refilling during the LOM process. Meanwhile, the exfoliation of adjacent cations would occur on the surface of catalysts to achieve the compensated charge balance.[17] Such results can be confirmed by the higher dissolution rate of electrochemically produced RuO_2 with enriched defects than that of thermally formed RuO_2.[96] Nonetheless, whether the involvement of lattice oxygen indeed brings about inferior durability for Ru-based catalysts remains open. On the contrary, Tian *et al.* reported a Co-doped RuO_2 catalyst with enriched oxygen vacancies with an ultra-high acidic OER performance obeying the LOM mechanism. Moreover, they thought that the greatly enhanced durability of Co-doped RuO_2 was closely related to the LOM pathway, and the over-oxidation of Ru to dissolved RuO_4 species was due to the participation of the oxygen vacancy (Fig. 4e).[97]

Based on the AEM mechanism, the binding energy of different reaction intermediates is linearly correlated by the so-called scaling relationships, thus resulting in a smallest theoretical overpotential of 0.37 V, which essentially limits catalytic activity.[98] In order to avoid the limitation of the theoretical overpotential in the AEM and the poor stability due to the participation of oxygen vacancies in the LOM, Lin *et al.* reported an advanced acidic OER catalyst with atomically dispersed Ru on α-MnO_2, involving only *O and *OH species serving as intermediates and allowing the O–O radical to produce O_2 without the formation of oxygen vacancies (Fig. 4f).[99] Beyond expectation, such a Ru-based catalyst can exhibit superior activity as low as 161 mV at 10 mA cm^{-2} and remarkable durability without overpotential variation over 200 h. All in all, enhancing stability without sacrificing activity needs reducing the bulk oxygen diffusion rate and surface exchange kinetics whether following the LOM or bypassing the AEM and LOM.

3. Attempts to enhance the OER performance of Ru-based electrocatalysts

To date, various Ru-related materials have been explored for enhanced acidic OER performance. Table 1 presents a representative list of the reported Ru-based acidic OER catalysts. This section provides a review of the progress in Ru-based materials, including metallic Ru, Ru-based oxides, and Ru-based oxometallates, toward acidic OER and highlights the mechanism of improved performance.

3.1 Optimization of metallic Ru

To improve the overall OER catalytic performance of Ru metals in acidic media, efficient strategies need to be adopted to increase their accessible active sites and resistance to corrosion, such as facet engineering, strain engineering, alloying engineering, synergistic effects, and single atom engineering.

Facet engineering. Note that the crystallographic orientations are closely related to the exposed accessible active sites, atomic arrangement, defects, *etc.*, which strongly influence the catalytic performances.[41,100] For instance, Poerwoprajitno *et al.* reported that Ru-branched nanoparticles possessed controllable surface facets with different catalytic performances.[100] Detailedly, they prepared polycrystalline Ru nanoparticles by using a mass of dodecylamine surfactant and Ru branches with low-index facets exposed by using a small amount of dodecylamine surfactant (Fig. 5a). Interestingly, the faceted Ru nanoparticles delivered much superior activity and stability compared with polycrystalline Ru nanoparticles (Fig. 5b), which was because the dissolution of Ru was suppressed on the low-index facets. In addition, it has been demonstrated that Ru with a face-centered cubic (fcc) structure is attractive for many reactions; nevertheless, it is difficult to be synthesized by traditional strategies due to its specific surface free energies. As a breakthrough, Zhao *et al.* successfully prepared fcc Ru

Table 1 Summary of representative Ru-based electrocatalysts toward acidic OER

Classification	Catalysts	Electrolyte	Overpotential (mV) at 10 mA cm^{-2}	Tafel slope (mV dec^{-1})	Stability	Ref.
Metallic Ru	Faceted Ru branched nanoparticles	0.1 M $HClO_4$	180	52	4 h@10 mA cm^{-2}	100
	L-Ru	0.5 M H_2SO_4	202	69.6	10 h@10 mA cm^{-2}	103
	Co-RuIr	0.1 M $HClO_4$	235	66.9	25 h@10 mA cm^{-2}	42
	RuMn	0.5 M H_2SO_4	—	—	720 h@10 mA cm^{-2}	107
	RuIr@CoNC	0.5 M H_2SO_4	223	45	40 h@10 mA cm^{-2}	110
	$Ni_{cluster}$-Ru NWs	0.5 M H_2SO_4	205	—	—	111
	Ru/RuS_2	0.5 M H_2SO_4	201	47.2	3000 cycles	112
	$Ru@IrO_x$	0.05 M H_2SO_4	282	69.1	24 h@10 mA cm^{-2}	113
	$Ru@MoO(S)_3$	0.5 M H_2SO_4	226	51	—	114
	Ru–N–C	0.5 M H_2SO_4	267	52.6	30 h@1.5 V *vs.* RHE	118
	Ru/Co-N-C	0.5 M H_2SO_4	232	—	20 h@10 mA cm^{-2}	119
	Ru/MnO_2	0.1 M $HClO_4$	161	29.4	200 h@10 mA cm^{-2}	99
	Ru_1-Pt_3Cu	0.1 M $HClO_4$	220	—	28 h@10 mA cm^{-2}	44
Ru-based oxides	RuO_2 NSs	0.5 M H_2SO_4	199	38.2	20 000 s@10 mA cm^{-2}	122
	UfD-RuO_2/CC	0.5 M H_2SO_4	179	36.9	20 h@1.42 V *vs.* RHE	123
	Ru-UiO-67-bpydc	0.5 M H_2SO_4	200	78.3	140 h@50 mA cm^{-2}	54
	RuO_2-WC NPs	0.5 M H_2SO_4	347	88.5	10 h@10 mA cm^{-2}	124
	Ru@V-RuO_2/C HMS	0.5 M H_2SO_4	176	45.6	10k cycles	125
	$RuNi_2$©G-250	0.5 M H_2SO_4	227	65	24 h@10 mA cm^{-2}	126
	RuO_2/D-TiO_2	0.5 M H_2SO_4	180	43	—	127
	$RuO_2/(Co,Mn)_3O_4$	0.5 M H_2SO_4	270	77	24 h@10 mA cm^{-2}	128
	Au@Pt@RuO_x nanowires	0.1 M $HClO_4$	215	65.5	40 h@10 mA cm^{-2}	129
	a/c-RuO_2	0.1 M $HClO_4$	205	48.6	60 h@10 mA cm^{-2}	49
	Rh-RuO_2	0.5 M H_2SO_4	161	45.8	700 h@50 mA cm^{-2}	56
	$Re_{0.06}Ru_{0.94}O_2$	0.1 M $HClO_4$	190	45.5	200 h@10 mA cm^{-2}	51
	75-H-RuO_2	0.5 M H_2SO_4	200	71	20 h@10 mA cm^{-2}	147
	B-RuO_2	0.5 M H_2SO_4	200	55	12 h@10 mA cm^{-2}	149
	Si-RuO_x@C	0.5 M H_2SO_4	220	53	100 h@10 mA cm^{-2}	152
	SS Pt-RuO_2 HNSs	0.5 M H_2SO_4	228	51	100 h@10 mA cm^{-2}	153
	S-$RuFeO_x$	0.1 M $HClO_4$	187	40	50 h@1 mA cm^{-2}	133
	$Ru_{0.85}Zn_{0.15}O_{2-\delta}$	0.5 M H_2SO_4	190	42	50 h@10 mA cm^{-2}	136
	$SnRuO_x$	0.5 M H_2SO_4	194	38.2	100 h@250 mA cm^{-2}	82
	$Li_{0.52}RuO_2$	0.5 M H_2SO_4	156	83.3	70 h@10 mA cm^{-2}	45
Ru-based oxometallates	$Y_2Ru_2O_{7-\delta}$	0.1 M $HClO_4$	190	55	8 h@1 mA cm^{-2}	154
	Mo-YRO	0.1 M $HClO_4$	240	40.45	30 h@10 mA cm^{-2}	158
	$Sr_2(Ru_{0.5}Ir_{0.5})O_4$	0.1 M $HClO_4$	8.06 mA cm^{-2} @ 1.55 V *vs.* RHE	47	24 h@10 mA cm^{-2}	161
	$SrRu_{0.5}Ir_{0.5}O_3$	0.5 M H_2SO_4	185	35	50 h@10 mA cm^{-2}	162
	$Sr_{0.90}Na_{0.10}RuO_3$	0.1 M $HClO_4$	170	—	—	163
	$CaCu_3Ru_4O_{12}$	0.5 M H_2SO_4	171	40	24 h@10 mA cm^{-2}	138
Ru chalcogenides/boride	a-$RuTe_2$ PNRs	0.5 M H_2SO_4	245	—	—	164
	RuB_2	0.5 M H_2SO_4	223	39.8	10 h@10 mA cm^{-2}	165

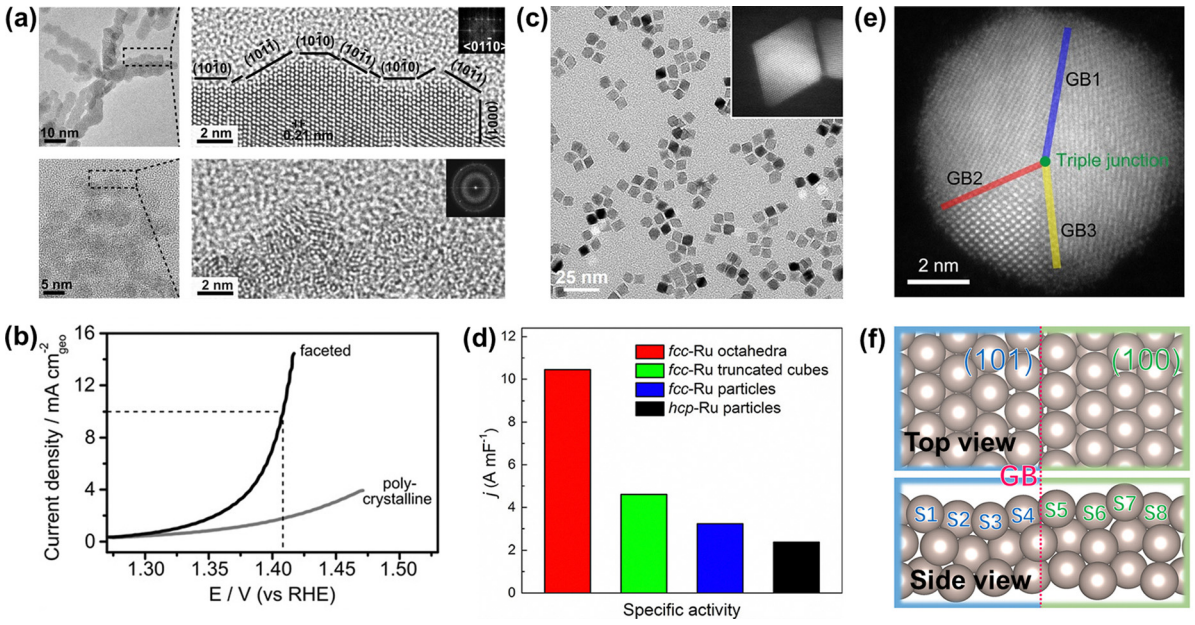

Fig. 5 (a) TEM image of faceted Ru branched nanoparticles (top) and polycrystalline Ru nanoparticles (bottom). (b) Potentiodynamic curves of the OER performance of faceted Ru branched nanoparticles and polycrystalline Ru nanoparticles.[100] (c) TEM image of the Ru octahedral nanocrystals and (inset) HAADF-STEM image of an individual Ru octahedron. (d) Summary of the specific activity of different Ru catalysts toward oxygen evolution.[41] (e) HAADF-STEM images of Ru nanoparticles with grain boundaries. (f) Atomic model of Ru(101)–Ru(100) grain boundaries.[103]

nanoparticles with controlled (111) facets by using the seed-mediated growth with Rh cubes as seeds (Fig. 5c).[41] Furthermore, the obtained Ru nanocrystals showed higher thermal stability and 4.4-fold specific activity compared with hcp-Ru nanoparticles for OER (Fig. 5d). Thus, facet engineering was demonstrated to be an effective strategy to design advanced Ru-based catalysts with controllable crystallinity and surface configuration.

Strain engineering. The strain effect is mainly beneficial to optimize the overall electrocatalytic performance of catalysts, owing to its well-adjusted electronic properties for catalysts and optimization of the binding energies for adsorbates.[101–103] For example, Ru nanoparticles with enriched grain boundaries coupled with compressive strain were synthesized successfully *via* using the laser-ablation-in-liquid technique by Wang *et al.* (Fig. 5e).[103] The as-obtained sample as an OER catalyst showed a low overpotential of 202 mV at 10 mA cm^{-2} in acidic media and superior durability for 10 h compared with commercial RuO_2 (305 mV@10 mA cm^{-2}, less than 6 h). From the experimental analysis and theoretical calculations, the compressive strain induced by grain boundaries promoted the reduction of the d-band center and the binding energy of reaction intermediates, thus enhancing the electrocatalytic activity (Fig. 5f). Furthermore, the low d-band center caused by strain engineering would lead to the additional repulsion of oxygen-related species, improving the surface oxidation resistance of Ru nanoparticles to enhance their stability. Such engineering has become an effective tool to improve the performances of various electrocatalysts. Of note, at present, there are limited studies of strain engineering on Ru metal, which remains a very worthy direction for us to study.

Alloying engineering. Alloying with foreign metal elements is proven to be an effective means to improve the catalytic properties owing to the lattice parameter mismatch, adjustment of the coordination environment, and charge redistributions.[42,104–106] It has been confirmed that the drastic dissolution of Ru leads to much inferior stability for Ru metals during the acidic OER process, which can be enhanced by alloying the heterometal elements. For example, Forgie *et al.* have investigated the OER activity of seven binary Ru-based alloys. The experiment results showed that Ru–Cu, Ru–Ir, and Ru–Co alloys were hexagonal and cubic mixed phase and all their activity was improved, owing to the chemisorption energy modulation of oxygen caused by the secondary metal component.[104] Further, Danilovic *et al.* reported an advanced $Ru_{0.5}Ir_{0.5}$ alloy with balanced activity and stability in an acidic medium *via* a surface segregation method to atomically tailor the near-surface composition (inset in Fig. 6a).[105] As shown in Fig. 6a, the excellent stability was attributed to the generation of the Ir-skeleton layer by thermal annealing, resulting in the suppressed dissolution of Ru atoms during the acidic OER process. Jiang *et al.* fabricated an atomic equidistributed $Ru_{0.5}Ir_{0.5}$ alloy catalyst, exhibiting great catalytic performances when acting as an OER catalyst in acidic media.[106] They found that the charge redistribution on the surface of the catalyst was promoted by the weak electronic coupling between Ru and Ir, resulting in Ru serving as the active site to enhance catalytic activity. Moreover, the atomic equidistribution in the alloy contributed to oxygen species occupying the vacancy formed from Ru leaching, while the oxygen species can bind well the adjacent Ir atoms. This result led to the formation of an Ir-protective skeleton to significantly suppress the further

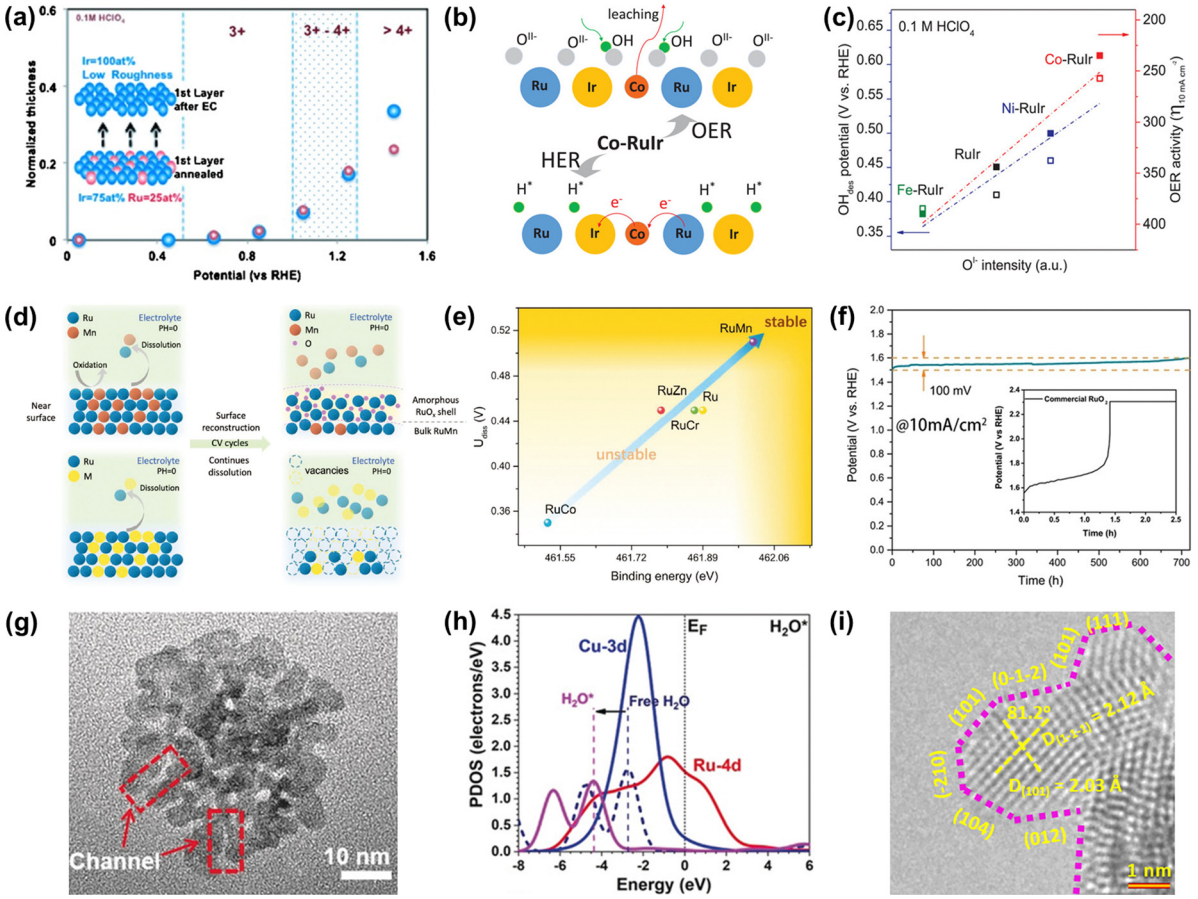

Fig. 6 (a) Relationships between the surface oxidation state of annealed $Ru_{0.5}Ir_{0.5}$ and Ir skeleton formation during OER.[105] (b) Schematic of the OER mechanism on the Co-RuIr electrocatalyst in acidic media. (c) Relationships between O^{I-} species concentration and OH desorption (OH_{des}) potential, and OER activity.[42] (d) Schematic of surface reconstruction of RuMn (top) and dissolution of unstable Ru-based alloys (below) in acidic media during CV cycles. (e) The relationships between durability and binding energy (Ru). (f) The CP curve of RuMn and commercial RuO_2 at 10 mA cm^{-2}.[107] (g) High-magnification TEM image of RuCu NSs. (h) The PDOS of H_2O adsorption on RuCu NSs.[108] (i) HRTEM image of RuIr nanocrystals (atomic steps are indicated with pink dotted lines).[110]

dissolution of Ru atoms, thus ensuring the excellent stability of the $Ru_{0.5}Ir_{0.5}$ alloy catalyst.

Except for the Ir-armour structures, the introduction of nonprecious transition metals is able to not only further improve catalytic activity but also greatly reduce the consumption of noble metals. For instance, Shan *et al.* reported a Co-RuIr catalyst with a small overpotential of 235 mV at 10 mA cm^{-2} for OER in acidic media, much superior to that of RuIr (344 mV), which was due to the increased concentration of O^{I-} species caused by the dealloying of the Co element, greatly enhancing OER catalytic activity (Fig. 6b).[42] In addition, Ni-RuIr and Fe-RuIr electrocatalysts were also prepared to build the composition–activity relationship, showing that both OH^- desorption peak positions and OER activity are linear with the intensity of O^{I-} species (Fig. 6c), which suggested that the concentration of oxygen species predicted the trend of OER activity.

Notably, although dealloying-caused surface reconstruction will complicate the reaction sites, it can be a win–win situation in terms of increased overall catalytic performance if utilized properly. For example, An *et al.* reported that a series of Ru-based alloys were prepared by doping with Mn, Zn, Cr, and Co and then subjected to dealloying treatment by the CV cycle test.[107] Thereinto, RuMn showed superior anti-corrosion and anti-oxidation properties during the acidic OER process while other Ru-based alloys dissolved quickly in the process of dealloying treatment (Fig. 6d). This was because there was a controllable surface reconstruction process during the continuous CV cycle test along with the leaching of Mn species and the formation of an amorphous RuO_x surface. Theoretical calculations indicated that the strong binding energy of Ru in the RuMn alloy could cause a highly stable structure (Fig. 6e). More attractively, the RuMn alloy catalyst exhibited a very competitive stability over 720 h at 10 mA cm^{-2} (Fig. 6f).

In addition, alloying engineering coupled with other strategies can further significantly improve the catalytic performance of Ru-related catalysts. For example, Huang's group reported channel-enriched RuCu nanosheets as acidic OER catalysts with enhanced electrochemical performance (Fig. 6g).[108] DFT calculations indicated that the channel-enriched structures

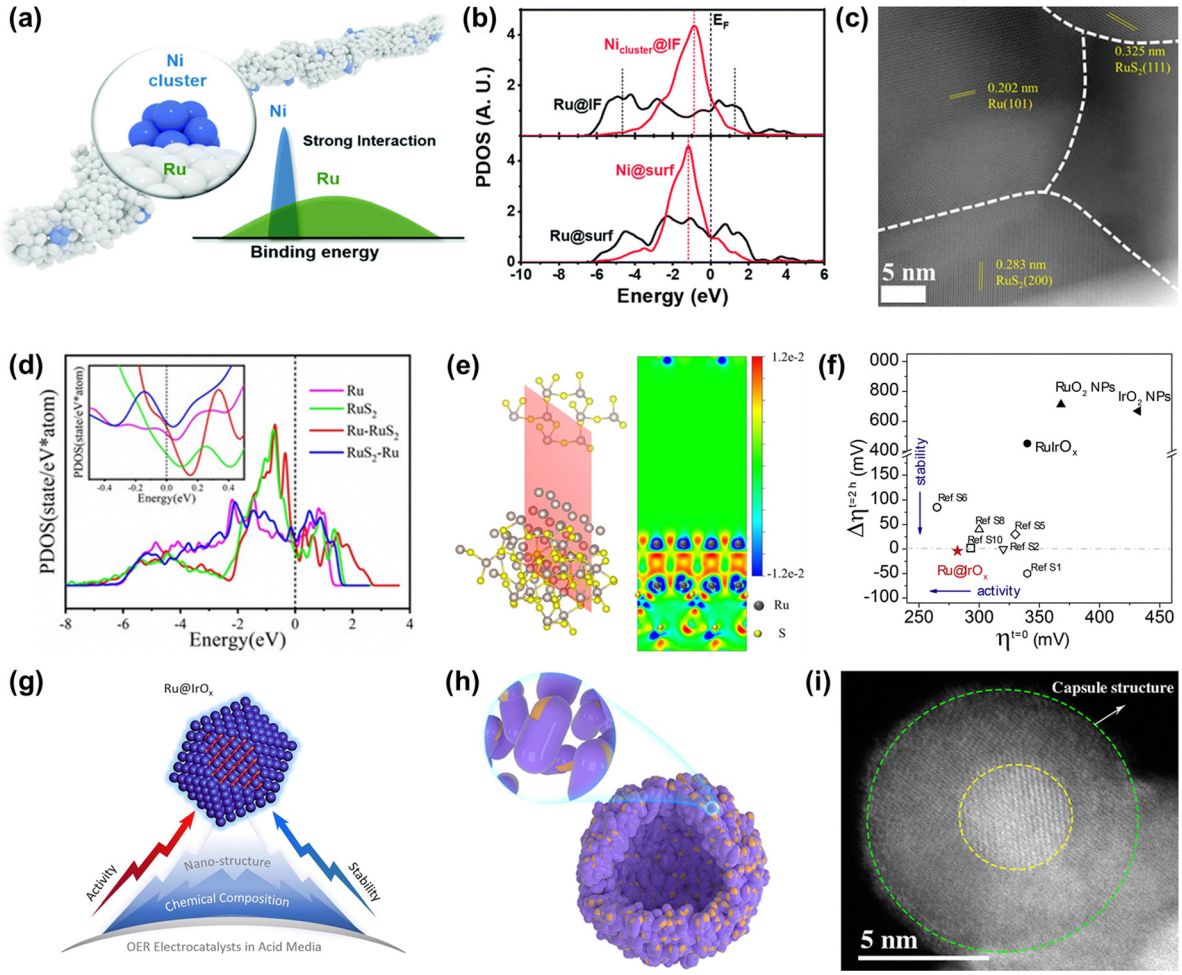

Fig. 7 (a) The schematic diagram of the diluted Ni nanocluster on Ru nanowires. (b) The PDOS comparison of Ru-4d and Ni-3d bands at the interface and surface.[111] (c) ac-STEM image of Ru/RuS_2. (d) PDOS of surface Ru sites on as-built models. (e) Charge density difference of the two-dimensional slice on the RuS_2-Ru model.[112] (f) Stability–activity plot for various OER electrocatalysts. (g) Diagram of the core–shell Ru@IrO_x heterostructure nanocrystal.[113] (h) Schematic diagram of the nano-capsule structure of Ru@$MoO(S)_3$. (i) HAADF-TEM image of Ru@$MoO(S)_3$.[114]

could not only activate the electron on the catalyst surface, but also lead to obvious lattice distortion around the channel area, thus greatly reducing the energy consumption of bond-dissociation for intermediates during the acidic OER process (Fig. 6h). They also reported Mn-doped ultrathin Ru nanosheet branches as a significantly active and stable catalyst toward acidic water splitting.[109] Xu *et al.* reported an OER catalyst comprising atomic-step enriched RuIr nanoparticles supported on the novel MOF-derived carbon (Fig. 6i), delivering a low overpotential of 223 mV and remarkable durability without notable degradation up to 40 h at 10 mA cm^{-2} in an acidic electrolyte.[110] Detailed experimental characterization coupled with theoretical calculations indicated that a strong chemical bond was formed between the pyrrolic-N sites on the skeleton and RuIr nanocrystals to provide a good solubility resistance during the acidic OER. Meanwhile, the unique atomic steps could fully expose the active sites and optimize the rate-determining step of OER, thus improving the catalytic activity. All in all, alloying engineering can enhance both activity and stability of Ru-based metal catalysts *via* the effective optimization of the electronic structure.

Synergistic effects. When the metallic Ru is coupled with other materials to form heterostructured catalysts, there will be synergistic effects in the new effective heterostructured catalysts, which can greatly increase the electrocatalytic activity and stability of Ru-based catalysts.[111–114] For instance, Zhu *et al.* reported diluted Ni nanocluster-decorated Ru nanowires (Fig. 7a), showing high catalytic performances when explored as an acidic OER electrocatalyst.[111] Experimental data and DFT calculations indicated that the robust interaction between the Ni nanocluster and the Ru surface can not only maintain the high electrical activity of the Ni 3d bands (Fig. 7b), but also accelerate electron transfer and enhance the durability. Mu *et al.* reported a heterostructured Ru/RuS_2 nanosheet that was synthesized through an isochronous reduction-sulphuration way (Fig. 7c).[112] When used as an acidic OER catalyst, such material exhibited a low overpotential of 201 mV at 10 mA cm^{-2} and superior durability without obvious activity change after

successive 3000 CV tests. Theoretical calculations indicated that the heterostructure with higher density states at the Fermi level ensured quick electron transfer during the OER process (Fig. 7d). Moreover, there was a strong charge redistribution at the interfaces (Fig. 7e), which greatly modulated the adsorption behavior of key intermediates, hence ensuring the favorable OER kinetics on heterostructures.

Among the various heterostructures, the core–shell structure can protect the core from oxidation and corrosion more effectively, guaranteeing higher stability. Recently, Shan and co-workers reported a core–shell heterostructured OER catalyst composed of a partially oxidized Ir shell and a greatly disordered and strained Ru core ($Ru@IrO_x$) that displayed an overpotential of 282 mV at 10 mA cm^{-2} and good stability over 24 h under acidic conditions, much superior to that of RuIr oxide alloy ($RuIrO_x$) nanocrystals (Fig. 7f).[113] They found that the charge was greatly redistributed at the Ru-core and IrO_x-shell interface, which increased the valence state of Ir and reduced the valence state of Ru to form favorable surface chemical states, therefore increasing the catalytic activity. Also, the improved stability was due to the synergistic effect from the unique core–shell heterojunction as well as induced charge redistributions (Fig. 7g). Detailedly, XPS and HAADF-STEM images of $Ru@IrO_x$ after the test indicated that the stable chemical states contributed to preventing the generation of dissolvable high-valence intermediate species and the core–shell nanostructure protected active Ru sites from loss in acidic media. In addition to the protection of the Ir-based shell, Ru encapsulated by a transition metal-based shell is demonstrated to be a cheap and effective strategy to design highly advanced Ru-based catalysts. Mu's group designed and prepared a core–shell structured catalyst $Ru@MoO(S)_3$ (Fig. 7h and i), which displayed a high catalytic performance in the acidic OER process, owing to not only Ru acting as a highly active site but also due to it being protected by the $MoO(S)_3$ shell.[114] Therefore, designing heterostructures can not only achieve enhanced activity through charge redistribution at interfaces but also realize improved stability through strong interactions at the heterogeneous interfaces and also through the good protection from the stable enclosure.

Single atom engineering. To date, single atom catalysts have sparked great attention in various electrochemical reactions, which is attributed to their nearly 100% atomic utilization and subtle electron properties.[115] Nevertheless, the strong surface free energy of SACs leads to poor stability especially under acidic conditions, calling for suitable substrates and appropriate strategies to perfectly anchor the isolated atoms and produce stabilized configurations. As a response, numerous synthetic ways such as defect engineering, metal–support interaction, heteroatom tethering, *etc.* have been explored and various supports including carbon materials, transition metal oxides, and so forth have also been put into use.[116,117]

Recently, Cao and co-workers prepared atomically dispersed Ru_1-N_4 moieties immobilized on a N-carbon substrate (Ru–N–C). When Ru–N–C was used as an acidic OER catalyst, it showed a low overpotential of 267 mV at 10 mA cm^{-2} with persistent and stable working over 30 h.[118] They found that there was reversible dynamic adsorption/desorption of a single oxygen atom on the Ru_1-N_4 sites with the formation of O-Ru_1-N_4, and the generation of a higher valence state of Ru during the *in situ* operation through operando XAS and SR-FTIR (Fig. 8a and b). DFT results indicated that more charge donations occurred from the Ru 4d state to the N 2p state, further suggesting that the formation of O-Ru_1-N_4 sites contributed to OER activity and stability (Fig. 8c). Further, Rong *et al.* regulated the electronic structure and catalytic performances of the atomically anchored Ru active sites by the introduction of another atomically dispersed Co site (Fig. 8d).[119] Namely, they prepared atomical Ru and Co dual-sites dispersed on N-carbon (Ru/Co-N-C), exhibiting a small overpotential of 232 mV and remarkable stability over 20 h with stable activity for OER at 10 mA cm^{-2} in an acidic medium. DFT calculations demonstrated that the incorporation of Co-N4 sites into Ru/Co-N-C not only significantly tuned the electronic properties of Ru sites through increasing Ru–O covalency but also promoted the electron transfer from C/N atoms to Ru. Therefore, the binding energy of reaction intermediates was greatly optimized to enhance OER activity and the electron around Ru-N4 was well redistributed to enhance the resistance to corrosion of Ru/Co-N-C (Fig. 8e and f).

Note that although the carbon skeleton contributes to anchoring and protecting single atoms from unwanted agglomeration, the thermodynamical property of carbon materials under oxidation potential is not stable, which will result in the configuration damage of single atoms.[30] Fortunately, it has been demonstrated that Sb/Ti/Sn/Ge/Mo/W-based oxides possess strong resistance to oxidation and dissolution in the acidic OER process.[120] Moreover, γ-MnO_2 can work as an acidic OER catalyst over 8000 h, though tested under low current density, making it act as a potential acid-resistant support.[121] If the Ru atoms can be coupled well with these acid-stable supports, it will not only reduce the consumption of Ru elements but also improve the stability of single atom Ru-related catalysts. For example, Lin *et al.* reported an advanced OER catalyst with Ru atom chains anchored on α-MnO_2 (Ru/MnO_2) through a cation exchange method.[99] Time-dependent elemental analysis revealed that the *in situ* dynamic cation exchange reaction occurred during the OER process. This dynamic reaction not only led to the formation of Ru atom arrays but also preserved the catalyst from metal-leaching-induced dissolution (Fig. 8g). Owing to the shorter interatomic Ru–Ru distance in Ru/MnO_2, such catalyst followed the oxide path mechanism to ensure high activity as discussed above in Fig. 4f. As a consequence, Ru/MnO_2 displayed an overpotential as low as 161 mV at 10 mA cm^{-2} and excellent long-term stability of more than 200 h under acidic OER conditions.

Other than non-noble transition metal oxides, noble metal-based skeletons are also promising supports to atomically anchor and disperse Ru atoms, except for the limitation of high price. Yao *et al.* reported a group of $PtCu_x$/Pt skin core–shell structures with embedded Ru atoms on account of the epitaxial growth of nano-island formation of $PtCu_x$ from the Cu

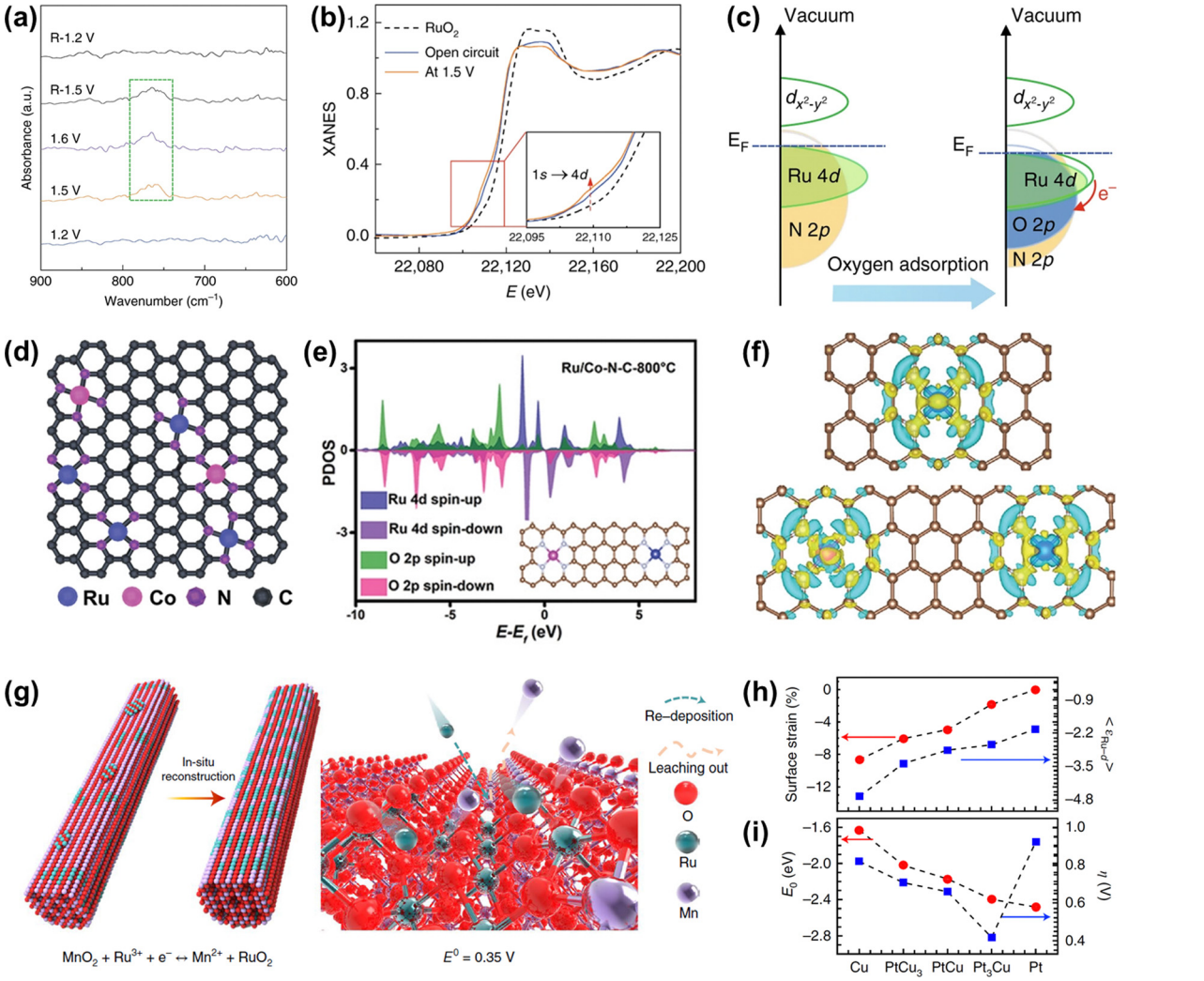

Fig. 8 (a) Operando SR-FTIR spectroscopy measurements for Ru–N–C during the acidic OER. (b) Operando XANES spectra for Ru–N–C during OER. Inset: Magnified pre-edge XANES region. (c) Schematic illustration of the effect of oxygen adsorption on the electronic structure of Ru–N–C.[118] (d) Proposed structural model of Ru/Co-N-C. (e) PDOS of Ru/Co-N-C (the inset is the corresponding model). (f) Differential charge density at the atomical Ru centers between Ru and neighboring C/N atoms in Ru–N–C (top) and Ru/Co-N-C (below).[119] (g) Schematic illustration of the *in situ* reconstruction process of Ru/MnO_2. (h) In-plane lattice contraction relative to the Pt (111) pristine surface (red circles) and the corresponding d-band center ε_{Ru-d} of Ru1 (blue squares).[99] (i) Corresponding adsorption energy E_O of the oxygen atoms (red circles) and η (blue squares).[44]

nanowires.[44] *In situ* XAFS measurements indicated that the valence state of Ru_1 was almost unchanged during the OER process. During the acid etching and electrochemical leaching process, the gradual release of compressive strain in comparison to pristine Pt was conducive to increasing the Ru d-band center to approach the Femi level, resulting in the well-optimized oxygen adsorption energy (E_O), which ultimately leads to an inverse volcano-type relationship between the OER activity and the lattice constant (Fig. 8h and i). As a result, the best Ru_1-Pt_3Cu catalyst displayed an overpotential of 220 mV at 10 mA cm^{-2} and remarkable long-term stability, much better than that of commercial RuO_2. The enhanced stability was attributed to the occurrence of electron transfer from Pt to Ru as revealed by *in situ* XANES, which protected the Ru atoms from overoxidation and accompanying dissolution. Thus, single-atom engineering can not only reduce the consumption of precious Ru metal, but also endow single Ru atoms with unique coordination environments to ensure their superior overall acidic OER performances.

3.2 Optimization of Ru-based oxides

Strategies for improved performance of Ru-based oxides including morphology control, heterostructure construction, doping, substituting, and so forth have been confirmed to be effective.

Morphology control. Reducing particle size or nanosheet thickness is an effective strategy to increase the specific surface area, thus fully exposing active sites, while the structural defects will inevitably come along. For example, Zhao *et al.* have synthesized ultra-thin RuO_2 nanosheets with a thickness of 1–2 nm and with enriched Ru vacancy defects (RuO_2 NSs) *via* a molten salt method (Fig. 9a and b).[122] The obtained RuO_2 NSs showed a lower overpotential of 199 mV at 10 mA cm^{-2} and

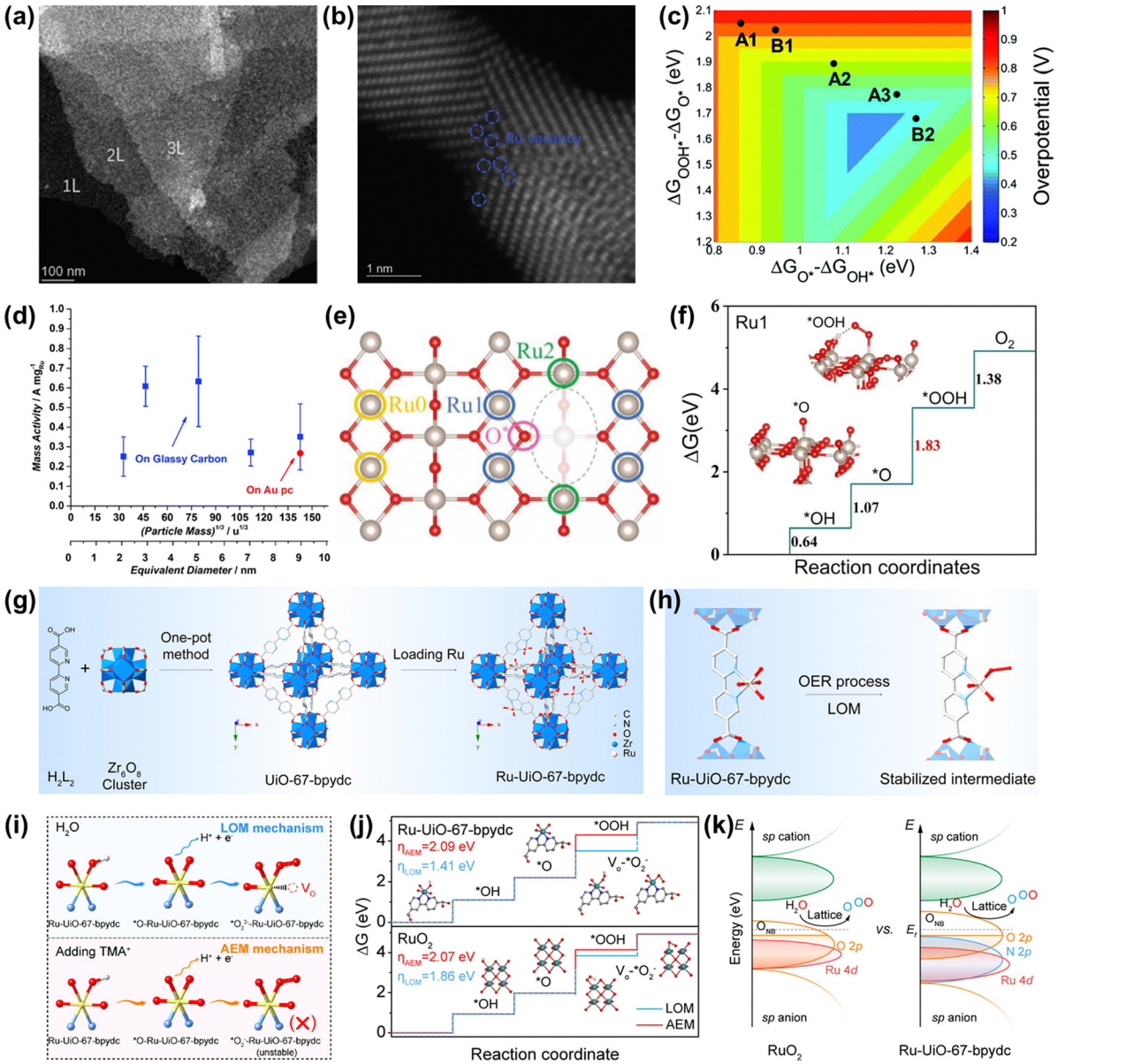

Fig. 9 (a) STEM images of RuO_2 NSs at a lower magnification. (b) Atomic STEM images of RuO_2 NSs. (c) Two-dimensional volcano plot constructed using the descriptors of $\Delta G_{O^*} - \Delta G_{OH^*}$ and $\Delta G_{OOH^*} - \Delta G_{O^*}$.[122] (d) OER mass activities of different thermally oxidized RuO_2 particle masses.[63] (e) The top view of the defective RuO_2 structure. (f) The calculated free-energy profiles of OER on the (a) Ru0, (b) Ru1, and (c) Ru2 sites.[123] (g) Scheme of the preparation of the Ru-UiO-67-bpydc catalyst. (h) The stability of the Ru intermediate in the MOF-anchored Ru oxide during the acidic OER by the LOM pathway. (i) Schematic illustration of the intermediate model in CV peaks with and without TMA^+. (j) Gibbs free energy illustration by Ru-UiO-67-bpydc and RuO_2 catalysts during the OER process by the AEM or LOM pathway. (k) Schematic molecular orbital energy diagram for Ru-UiO-67-bpydc and RuO_2 toward the acidic OER.[54]

much higher specific and mass activities at 230 mV compared with the commercial RuO_2. DFT calculations revealed that the existence of Ru vacancies on the surface of RuO_2 NSs remarkably reduced the energy consumption in the transformation of key reaction intermediates, hence significantly improving the catalytic activity (Fig. 9c). In addition, Paoli *et al.* have investigated the relationship between mass activity and particle size of RuO_2 by using mass-selected nanoparticles, revealing that the particle size of RuO_2 at about 3–5 nm displayed the optimum mass activity (Fig. 9d).[63] Combining the advantages of structure engineering and defect engineering, ultrafine defective RuO_2 nanoparticles with an average grain diameter of about 5 nm on carbon cloth were prepared, exhibiting a low overpotential of 179 mV at 10 mA cm^{-2} and a well-maintained activity for 20 h for acidic OER.[123] Theoretical calculations indicated that the presence of oxygen vacancies not only produced abundant active sites in RuO_2, but also optimized the electronic properties of unsaturated five-coordinated sites adjacent to oxygen

vacancies, thus enhancing the catalytic activity (Fig. 9e and f). Of note, the different optimal nanoparticle size may be due to the preparation techniques and coordination environments.

If the size of Ru oxides can be downsized to the atomic level, the catalytic performances will be significantly improved, due to the maximized atom utilization efficiency and unique electronic structure. Very recently, Yao *et al.* prepared an acidic OER catalyst of atomically dispersed Ru oxide on UiO-67-bpydc (Ru-UiO-67-bpydc) with robust Ru–N bonds through an effective metal-organic framework anchored strategy (Fig. 9g).[54] They thought that the sturdy coordinating pyridine ligands and the strong interaction between Ru oxide and the metal-organic framework could induce the motivated LOM pathway and stabilize the dissolvable high-valence oxygen-vacancy intermediate simultaneously, thus leading to the synchronously improved overall catalytic performance of Ru oxides (Fig. 9h). As a consequence, Ru-UiO-67-bpydc displayed a low overpotential of 200 mV and excellent stability without activity and structure degeneration over 115 h at 10 mA cm^{-2} under acidic conditions. The experimental results confirmed that the lattice oxygen was involved in the OER process *via* the LOM pathway (Fig. 9i and j). DFT calculations indicated that the robust Ru–N bonds led to the Ru d-band center far away from the Fermi level but the O 2p-band center close to the Fermi level, definitely enhancing the catalytic performances of Ru oxides (Fig. 9k). Therefore, an important way to improve the catalytic performance of Ru-based oxides is to design the structure of nanomaterials reasonably, so as to realize effective utilization of precious metals.

Heterostructure. Constructing heterogeneous structures has been demonstrated to be an effective strategy to not only promote electron redistribution but also induce synergistic effects at the interface, so as to realize enhanced catalytic performance for acidic OER. For example, Sun *et al.* developed an advanced OER catalyst of WC-supported RuO_2 nanoparticles (RuO_2-WC NPs) with strong catalyst–support interaction (Fig. 10a), showing a high mass activity of 1430 A $g_{Ru}{}^{-1}$, which greatly exceeded that of commercial RuO_2.[124] DFT calculations confirmed that the robust catalyst–support interaction at the interface between RuO_2 and WC promoted the electron transfer from W atoms to Ru atoms, resulting in an electron accumulation region around the Ru site. Meanwhile, the WC support optimized the binding energy of reaction intermediates on Ru sites to break the reaction barrier, thus enhancing the catalytic activity of RuO_2-WC NPs (Fig. 10b). Li *et al.* reported a core–shell heterostructure composed of oxygen defect-engineered RuO_2 sub-nanometer skin on the Ru core (Ru@V-RuO_2/C HMS, Fig. 10c).[125] There was a robust strain effect at the interfaces to accelerate the reaction kinetics and increase additional active sites (Fig. 10d). DFT calculations indicated that the core–shell heterostructure induced a lower d-band center and a smaller electron transfer between the catalyst surface and *O, hence reducing the adsorption energy of oxygen-related intermediates to enhance OER activity (Fig. 10e). Moreover, the elevated p-band center caused by the core–shell heterostructure suppressed the reaction activity of lattice oxygen, contributing to the improved structural stability during the OER process. Accordingly, Ru@V-RuO_2/C HMS displayed an ultrasmall overpotential of 176 mV at 10 mA cm^{-2} and a slight change of activity in the accelerated decay test with the curve after 5k cycles for OER in 0.5 M H_2SO_4. In addition, the Ru-based oxide–support interaction on $RuNi_2$@G-250 (Fig. 10f),[126] RuO_2/D-TiO_2 (Fig. 11g),[127] RuO_2/$(Co,Mn)_3O_4$ (Fig. 10h),[128] and Au@Pt@RuO_x (Fig. 10i)[129] was also demonstrated to be an effective strategy to optimize electron redistribution and enhance catalytic performances for acidic OER. In a word, heterogeneous structures can accumulate charge at the interface, which can endow rapid electron conduction ability and optimize the adsorption strength of oxygen evolution intermediates, so as to improve the catalytic activity of Ru-based oxides.

In addition to the strategies discussed above, another effective strategy is incorporating foreign metal atoms, such as alkali metals (Li,[45] Na,[49] *etc.*), transition metals (Ti,[130] Cr,[131] Mn,[132] Fe,[133] Ni,[55] Co,[134] Cu,[135] Zn,[136] *etc.*), main group metals (Mg,[137] Ca,[138] Sr,[139] *etc.*), noble metals (Pt,[140] Rh,[56] Ir,[141] *etc.*), acid-insoluble metals (Sn,[82] Pb,[142] *etc.*), and rare earth metals (La,[143] Ce,[144] Y,[145] Er,[146] *etc.*), and non-metallic elements (H,[147] C,[148] B,[149] S,[150] Se,[151] Si,[152] *etc.*) with Ru through doping and substitution or forming Ru-related pyrochlores and perovskites to greatly enhance the OER performances (Fig. 11). This part will be divided into the following aspects: cation doping, anion codoping, anion and cation codoping, and solid solution oxides.

Cation doping. Doping and substitution of foreign cations in Ru-based oxides have been proven to be pleiotropic ways to regulate structural and electronic structures with flexible composition and structure modulations. For example, our group reported a Na-doped and oxygen vacancy enriched amorphous/crystalline RuO_2 (a/c-RuO_2), exhibiting an excellent activity of 205 mV and superior stability in continuously catalyzing OER for 60 h with no activity degeneration over 60 h at 10 mA cm^{-2} in an acidic medium.[49] Operando XAS results indicated that the obtained a/c-RuO_2 possessed flexible structural distortions and redox reaction of Ru, which greatly enhanced the resistance to overoxidation and dissolution in the OER process (Fig. 12a). Theoretical calculations revealed that the incorporation of Na and oxygen vacancies induced the Ru d-band center far away from the Fermi level, which optimized the adsorption energy between reaction intermediates and the catalyst surface, thus reducing the reaction energy barrier for the OER (Fig. 12b). Wu *et al.* reported a Ni-doped RuO_2 (Ni-RuO_2) catalyst, which acted as an OER catalyst in PEM water electrolysis, showing much remarkable stability over 1000 h at 200 mA cm^{-2}.[55] Operando tests coupled with DFT studies confirmed that the introduction of Ni not only significantly stabilized the RuO_2 lattice but also greatly avoided the dissolution of surface Ru and subsurface oxygen for enhanced OER stability. By means of heteroatom doping, such as Na,[49] Ni,[55] Ti,[130] *etc.*, the d-band center can be kept far away from the Femi level and the lattice oxygen can be suppressed to obey the AEM mechanism, thus improving both catalytic activity and stability.

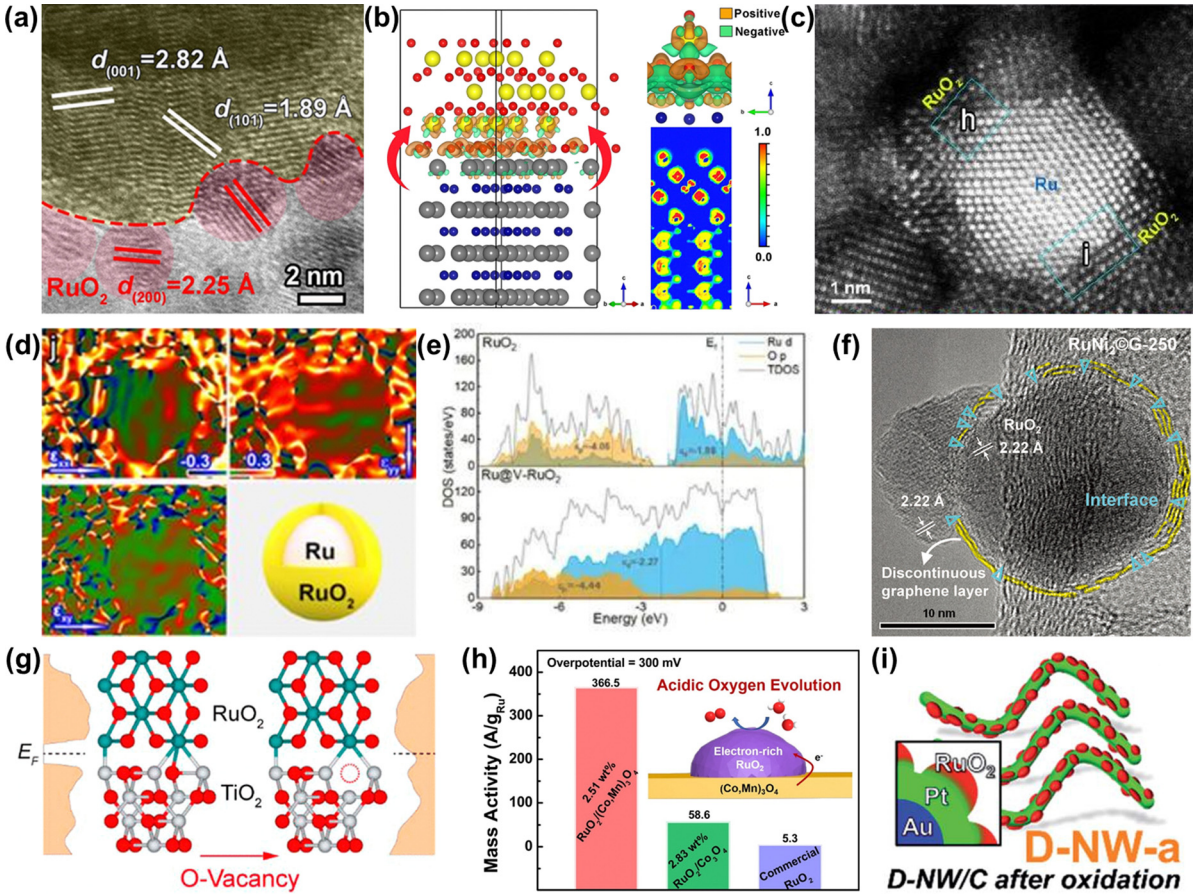

Fig. 10 (a) HRTEM image of RuO_2-WC NPs. (b) Optimized configuration of the RuO_2-WC interface derived from first-principles calculations.[124] (c) Aberration corrected HAADF-STEM and (d) the corresponding strain maps of Ru@V-RuO_2/C HMS. (e) The partial density of states projected on the p orbits of O atoms for RuO_2 (upper) and Ru@V-RuO_2 (bottom).[125] (f) HRTEM image of $RuNi_2$@G-250 with a unique interface between RuO_2 and graphene.[126] (g) Partial density of states for RuO_2/TiO_2 and RuO_2/D-TiO_2 interfaces.[127] (h) Schematic illustration and mass activity of RuO_2/$(Co,Mn)_3O_4$.[128] (i) Schematic illustration of Au@Pt@RuO_x.[129]

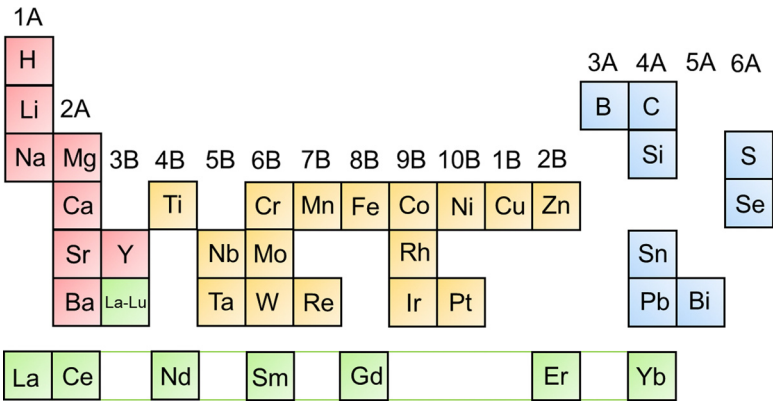

Fig. 11 The foreign elements in recently reported Ru-based oxides or oxometallates.

Unusually, Wang *et al.* recently reported an OER catalyst of Rh-doped RuO_2 on graphene (Rh-RuO_2/G), whose OER mechanism followed the lattice oxygen mediated mechanism-oxygen vacancy site mechanism (LOM-OVSM).[56] As a result, Rh-RuO_2/G delivered an ultralow overpotential of 161 mV at 10 mA cm^{-2} and remarkable long-term durability without obvious activity change over 700 h at 50 mA cm^{-2}. Experimental characterization analysis coupled with DFT calculations confirmed that the emerging oxygen species during the OER process were reversible, which greatly improved both intrinsic activity and crystal structure stability (Fig. 12c and d). DFT calculations indicated that the oxygen vacancies coupled with Ru–O–Rh active sites

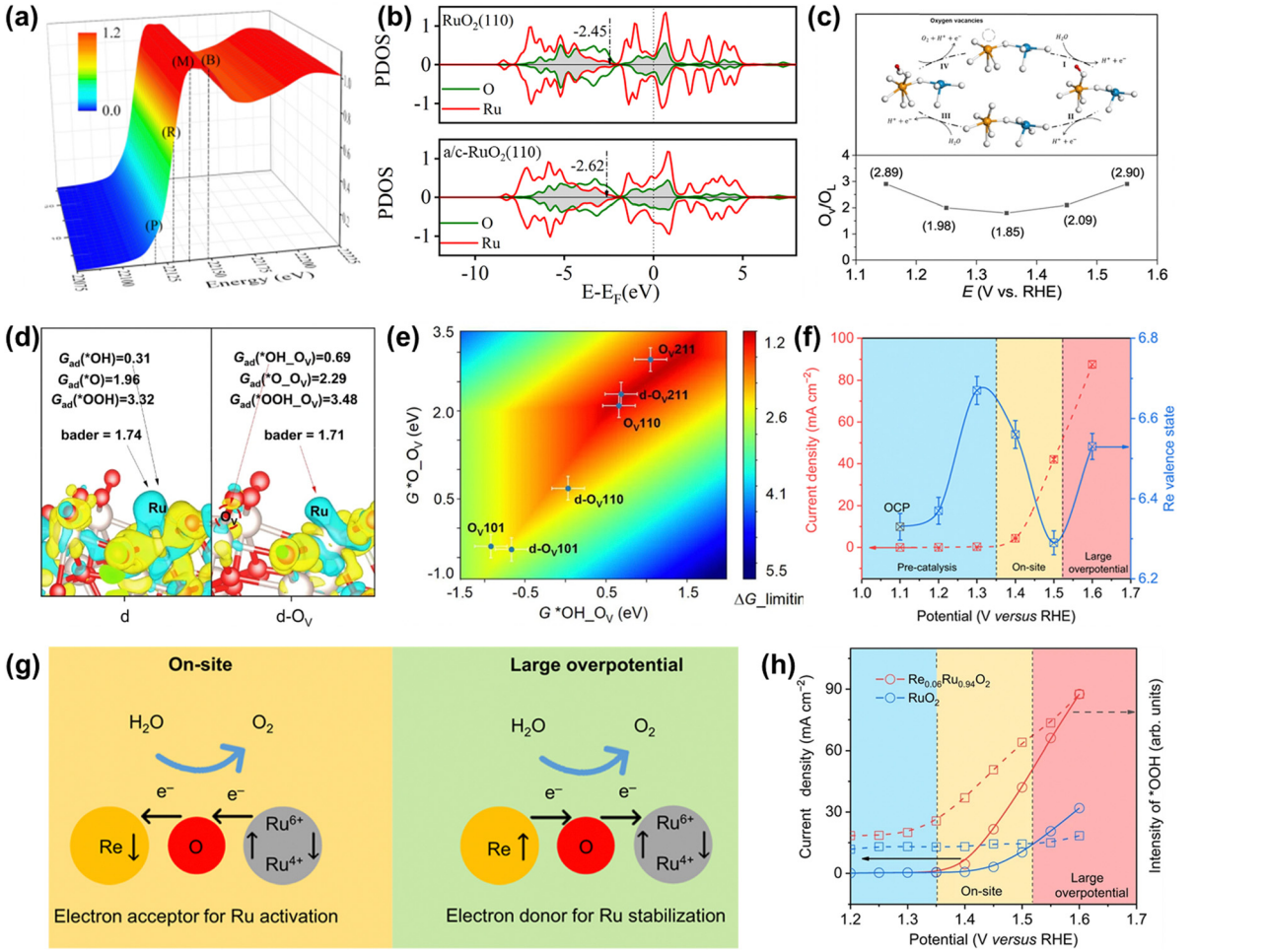

Fig. 12 (a) 3D plot of the operando Ru K-edge XANES spectrum of schematic illustration of a/c-RuO_2. (b) PDOS of d-bands of active Ru for RuO_2 and a/c-RuO_2.[49] (c) Variation of the O_V/O_L ratio from quasi *in situ* XPS measurements on Rh-RuO_2/G. (d) Charge density difference analysis for the d and d-O_V slab. (e) A two-dimensional activity map for the LOM-OVSM mechanism based on OER.[56] (f) Change in the Re valence state and OER current as a function of the applied potential. (g) Schematic for dynamic electron transfer in $Re_{0.06}Ru_{0.94}O_2$. (h) Potential dependence of the band intensity of characteristic vibration adsorption of surface-adsorbed *OOH.[51]

made Rh-RuO_2/G follow the LOM-OVSM. In addition, the generation of *O on Ru–O–Rh active sites was the rate-determining step of Rh-RuO_2/G, which broke the barrier limitation (*OOH) of the AEM (Fig. 12e).

In addition to regulating the reaction mechanism, the electron transport form can also be adjusted to improve the overall catalytic performance. Very recently, Jin *et al.* found that the electron accepting–donating process in Re-doped RuO_2 ($Re_{0.06}Ru_{0.94}O_2$) was dynamic, completely different from the traditional static electron redistribution caused by the dopant, which significantly improved both activity and stability.[51] Operando XAS characterization indicated that the electron transfer between Re and Ru sites was highly correlated to the operating potential along with dynamic role change of the Re site (Fig. 12f). As detailedly shown in Fig. 12g, the Re sites accept electrons from Ru sites at the on-site potential to enhance the catalytic activity of Ru sites. In contrast, the electrons are transferred from Re atoms to Ru sites at a large overpotential to avoid the overoxidation of Ru and boost the stability of Ru sites. Moreover, *in situ* characterization and DFT calculations confirmed that the unique dynamic electron transfer promoted the transformation of the reaction pathway on $Re_{0.06}Ru_{0.94}O_2$ from LOM to AEM and optimized the binding energies of reaction intermediates, thus increasing catalytic performances (Fig. 12h). Moreover, aberration-corrected HAADF-STEM images and XAFS measurements of $Re_{0.06}Ru_{0.94}O_2$ after OER indicated that there was no aggregation or reconstruction of Re single atoms and no change of the valence state and coordination environment of Ru and Re atoms after the OER process. Thus, cation doping is demonstrated to be an effective way to optimize the electronic structures of Ru-based oxides to regulate the OER pathway.

Anion doping. In addition to cation doping, anion doping is demonstrated to be an effective strategy to improve the performance of RuO_2. For example, He *et al.* successfully introduced the hydrogen binding modes into the RuO_2 lattice, which induced the electronic interaction between Ru and O atoms and promoted the formation of hydrogen bonds, ensuring the

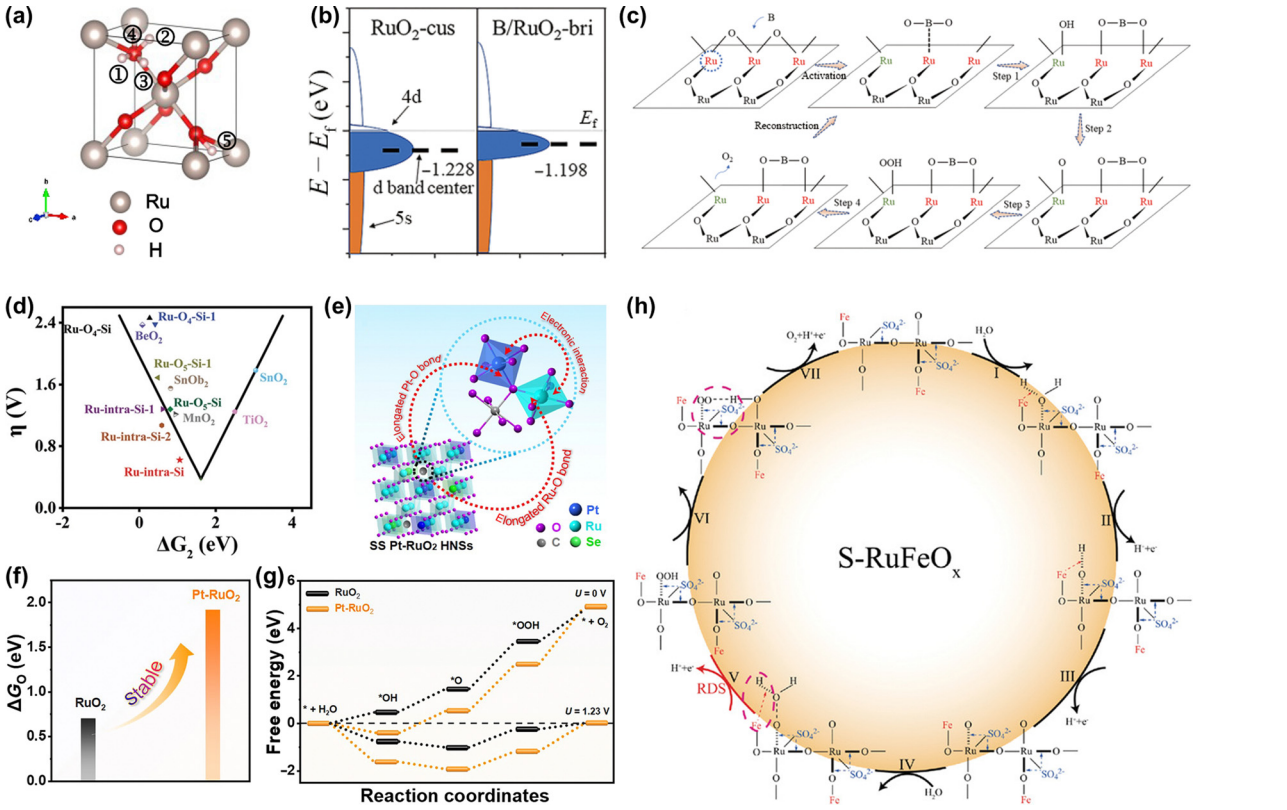

Fig. 13 (a) Structural illustration of proton and electron co-doped RuO_2.[147] (b) Schematic diagram of d-band center change of the Ru-bri site of B/RuO_2. (c) The schematic diagram of BO2 migration during OER.[149] (d) The calculated overpotential for Si-RuO_x@C in the "volcano" plot of overpotential *versus* ΔG_2 ($\Delta G_2 = \Delta G_{OH^*} - \Delta G_{O^*}$).[152] (e) Structural illustration of SS Pt-RuO_2 HNSs. (f) The calculated dissociation energy of *O in RuO_2 and Pt-RuO_2, respectively. (g) The free energy profiles of the OER process on RuO_2 and SS Pt-RuO_2 HNSs under the applied overpotential of 0 and 1.23 V (RHE), respectively.[153] (h) Schematic illustration of the reaction mechanism toward acidic OER on S-$RuFeO_x$.[133]

obtained catalyst with a low overpotential of 200 mV at 10 mA cm^{-2} (Fig. 13a).[147] Liu *et al.* developed a boron-doped RuO_2 (B-RuO_2) with an overpotential of 200 mV and remarkable durability over 12 h at 10 mA cm^{-2}.[149] DFT calculations indicated that the B dopant weakened the interaction between Ru atoms and O atoms to lift up the d-band center, thus increasing the binding energy between reaction intermediates and Ru sites (Fig. 13b). This coupled with advanced characterization revealed that the formed unusual B–O covalent bonding activated the bridge Ru site (Ru-bri site) to act as an active site, leading to fully exposed active sites, which greatly enhanced the catalytic activity of B-RuO_2 (Fig. 13c). In addition, Liu *et al.* prepared carbon-coated Si-doped RuO_x particles (Si-RuOx@C) from a nano-organic cage. When Si-RuO_x@C was used as an OER catalyst, it showed a low overpotential of 220 mV at 10 mA cm^{-2}, remarkable durability for 100 h, and stable CV energy after operating for 27 000 cycles in an acid electrolyte.[152] Theoretical calculations revealed that the Si dopant not only optimized the binding energy of oxygen-related intermediates but also served as an electron receiver from Ru to enhance the resistance to overoxidation, thus improving both activity and stability (Fig. 13d). Although great enhancements of activity and stability are achieved by using anion doping, the change of the doped anion atoms during the OER process requires further detailed research.

Anion and cation codoping. In addition, co-doping with both cation and anion elements can also greatly enhance both catalytic activity and stability. For instance, Wang *et al.* reported a single-site Pt-doped RuO_2 with interstitial C (SS Pt-RuO_2 HNSs), delivering a low overpotential of 228 mV and a stable overpotential over 100 hours at 10 mA cm^{-2} toward acidic OER (Fig. 13e).[153] Experimental characterization indicated that the bond lengths of Ru–O and Pt–O were simultaneously elongated by the interstitial C, and the electron distribution on RuO_2 was effectively optimized by the introduction of single-site Pt (Fig. 13f). DFT calculations confirmed that the strong synergy not only greatly increased the dissociation energy of *O species but also significantly reduced the energy barriers for OER, thus readily enhancing both catalytic activity and stability of SS Pt-RuO_2 HNSs (Fig. 13g). Xue *et al.* reported that codoping with the sulfate anion and Fe cation in RuO_2 (S-$RuFeO_x$) effectively enhanced the catalytic performances for acidic OER.[133] Detailed experiments revealed that the binding energy of the *OO–H intermediate was reduced by the doping of the sulfate anion and the deprotonation of H_2O was boosted by the doping of the Fe cation, thus promoting the catalytic activity of S-

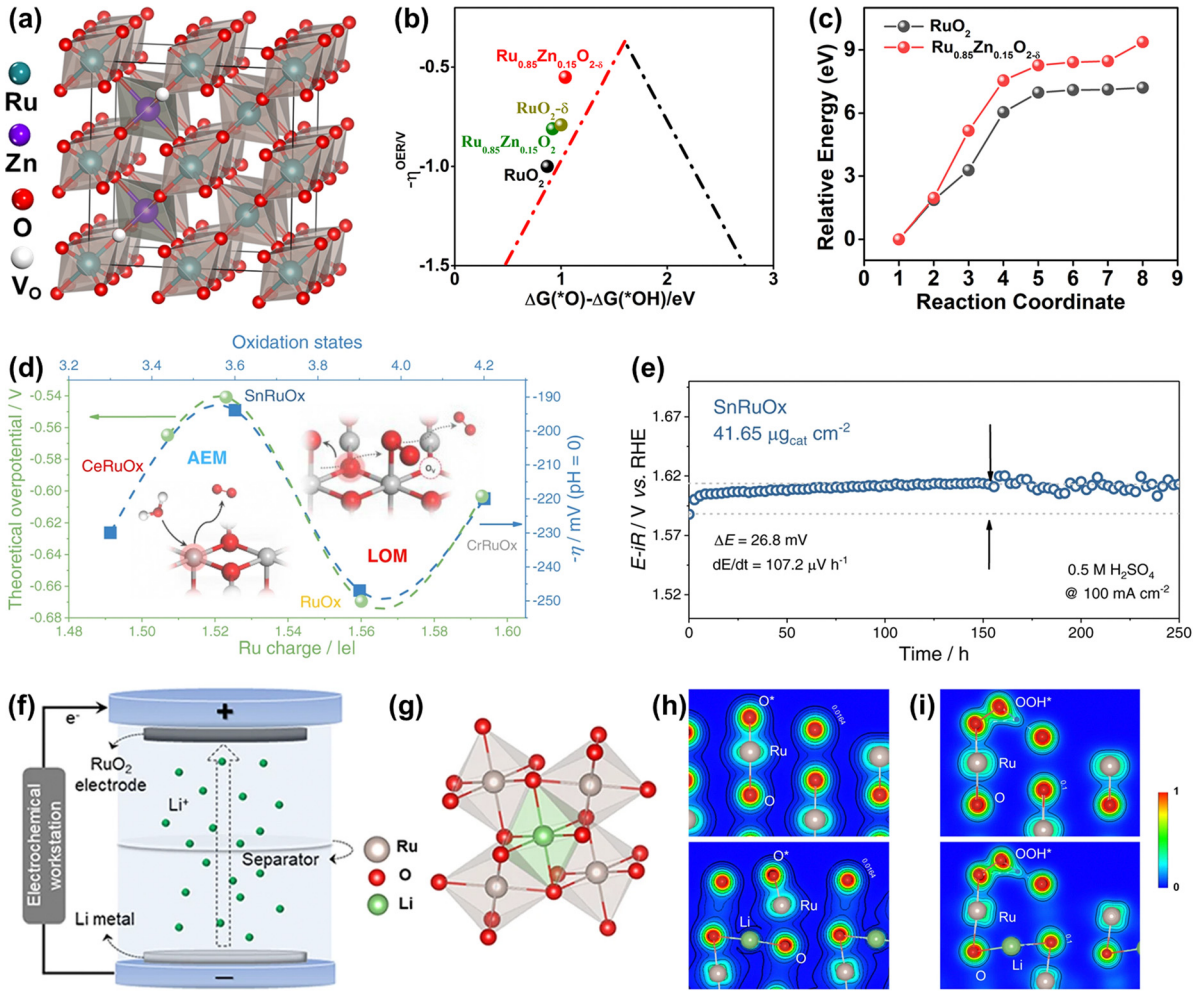

Fig. 14 (a) Crystal structure of rutile $Ru_{0.85}Zn_{0.15}O_{2-\delta}$. (b) The kinetic barrier for breaking the Ru–O bond in RuO_2(110) and $Ru_{0.85}Zn_{0.15}O_{2-\delta}$. (c) The calculated negative overpotential ($-\eta^{OER}$) plotted against the descriptor of ΔG(O*) − ΔG(*OH) on different catalysts.[136] (d) The variation of apparent overpotential at 10 mA cm^{-2} with Ru oxidation states. (e) Chronopotentiometry curve of the $SnRuO_x$ nanocatalyst operated at 100 mA cm^{-2} during the 250 h test.[82] (f) Schematic illustration of the preparation of lithium intercalated RuO_2. (g) RuO6 octahedron after lithium intercalation. (h) The charge density distribution of O* absorbed on the (110) surface of RuO_2 (up) and $Li_{0.5}RuO_2$ (down). (i) The charge density distribution of OOH* absorbed on the (110) surface of RuO_2 (up) and $Li_{0.5}RuO_2$ (down).[45]

$RuFeO_x$ (Fig. 13h). Moreover, the sulfate anion dopant prevented lattice oxygen well, hence enhancing the stability of S-$RuFeO_x$. Consequently, the obtained S-$RuFeO_x$ displayed a superior activity with an overpotential of 187 mV at 10 mA cm^{-2} and good stability during the 50 h of the chronopotentiometry test at 1 mA cm^{-2}.

Solid solution oxides. Doping with foreign atoms can produce a kind of unique polymetallic oxide: solid solution oxides with RuO_2 as a solid solvent. Recently, our group developed an oxygen-vacancy-enriched Ru–Zn solid solution oxide ($Ru_{0.85}Zn_{0.15}O_{2-\delta}$) *via* a molten salt method.[136] Based on the detailed structural characterization and analysis, we safely inferred that the obtained $Ru_{0.85}Zn_{0.15}O_{2-\delta}$ was constituted by tetragonally distorted RuO6 and ZnO6 octahedra with oxygen vacancies adjacent to Zn atoms as shown in Fig. 14a. In the solid solution, the existence of Zn atoms and oxygen vacancies not only reduced the Ru valence state, but also promoted the Ru d-band center far away from the Fermi level, resulting in a weaker free energy barrier for OER (Fig. 14b). Moreover, robust Zn-O-Ru local structures were formed to prevent Ru atoms from overoxidation and dissolution during the OER process, thus enhancing structural stability (Fig. 14c). As a result, the $Ru_{0.85}Zn_{0.15}O_{2-\delta}$ solid solution oxide showed a low overpotential of 190 mV and long-term stability with negligible activity degeneration over 50 h at 10 mA cm^{-2} towards acidic OER. In addition, tuning the chelating elements around RuO6 in solid solution oxides with controllable M–O–Ru (M = Ce, Sn, Ru, Cr) could precisely regulate the OER mechanism (Fig. 14c).[82] Notably, M^{4+} with various ionic electronegativity induced different electron redistribution in the M–O–Ru structure, resulting in the regulated Ru charge and adjustable reaction mechanisms. As a consequence, the customized $SnRuO_x$ solid solution, which followed the AEM with proper Ru–O binding energy, displayed a high mass activity of

2360 A g_{Ru}^{-1} at 1.48 V and superior long-term stability with small activity variation under 100 mA cm^{-2}. Other Ru-based solid solution oxides with the chelating elements adjacent to RuO6 like Cr-Ru solid solution oxide[131] and Mn-Ru solid solution oxide[132] have also been investigated for improved performance for acidic OER.

Different from the previously reported solid solution with the Ru cations replaced by foreign atoms, a unique $Li_{0.52}RuO_2$ solid solution oxide with Li ions intercalated into the octahedral interstices composed of six adjacent O atoms was synthesized by Qin *et al. via* the electrochemical lithiation process (Fig. 14f and g).[45] The Li ions intercalated into the lattice interstices induced the electron redistribution and local lattice distortion of RuO_2, reducing the valence state of Ru with the generation of the robust Li–O–Ru local structure, which prevented the dissolution of Ru and improved the stability. Note that the surface structural distortion caused by intrinsic lattice strain could motivate the dangling O atom surrounding the Ru active site to act as a proton receiver, which effectively anchored the OOH* to greatly improve the catalytic activity of $Li_{0.52}RuO_2$ solid solution oxide for acidic OER (Fig. 14h and i). The constructed $Li_{0.52}RuO_2$ delivered a record activity of 156 mV at 10 mA cm^{-2} and good stability with persistent operation for 70 h without obvious overpotential change. All in all, the Ru-based solid solution oxides, whether the M intercalates into the octahedral interstices or substitutes the position of Ru, deliver improved catalytic performance through the formation of unique M–O–Ru bonds.

3.3 Optimization of Ru-based oxometallates

Ru-based oxometallates, including pyrochlore- and perovskite-type ruthenates, have attracted widespread attention with their low Ru content and remarkable catalytic performances in acidic OER. The most effective strategy to improve the performance of pyrochlore- and perovskite-type ruthenates is substitution.

To expand acid-stable Ru-based catalysts with high activity for OER, Kim *et al.* produced a pyrochlore yttrium ruthenate ($Y_2Ru_2O_{7-\delta}$) by the sol–gel method, showing a low onset overpotential of 190 mV and high stability over 8 h at 1 mA cm^{-2} under acidic conditions.[154] The overall enhanced catalytic performance was due to the lowered Ru valence state and the reduced overlapped energy band center between Ru 4d and O 2p bands (Fig. 15a and b). Moreover, the superior structural stability of $Y_2Ru_2O_{7-\delta}$ during the acidic OER process was confirmed by the XPS, XAS and PXRD results. Recently, Hubert *et al.* prepared a series of $A_2Ru_2O_7$ (A = Y, Nd, Gd, Bi) as acidic OER catalysts and investigated the relationships between A-site elements and both the activity and stability.[146] They found that the initial OER activity of $A_2Ru_2O_7$ was higher than that of RuO_2, which was attributed to the elongated Ru–O bond length and the reduced binding energy between the Ru 4d and O 2p bands (Fig. 15c and d). Moreover, the property of the A-site element had a great impact on the Ru dissolution rates during the OER process, which was consistent with theoretical Pourbaix analysis, suggesting that such $A_2Ru_2O_7$ pyrochlores were thermodynamically unstable towards OER in acidic media (Fig. 15e). Theoretical activity predictions indicated that the OER activity was highly related to A-site cation leaching, revealing that A-site cation leaching fully exposed highly oxidized Ru sites to improve activity. Note that, all $A_2Ru_2O_7$ catalysts were proven to possess superior activity and stability than RuO_2, although not without dissolution.

To improve the catalytic performance of $A_2Ru_2O_7$ pyrochlore, the substitution of A or Ru with foreign elements has been demonstrated to be an effective strategy. For instance, Kim *et al.* reported a $Y_2[Ru_{1.6}Y_{0.4}]O_{7-\delta}$ porous pyrochlore oxide with partial substitution by Y^{3+} on the B-site (Fig. 15f), exhibiting a higher activity compared with $Y_2Ru_2O_{7-\delta}$ and RuO_2 references (Fig. 15g) for acidic OER.[155] The enhanced activity was due to both a high surface area and an optimized energy band structure caused by the B-site substitution. Feng and coworkers constructed an A-site substituted $Y_{1.85}Zn_{0.15}Ru_2O_{7-\delta}$ catalyst with a highly active and stable performance for acidic OER, which was attributed to the optimized electronic structure induced by the partial substitution of Y^{3+} ions with Zn^{2+} ions.[156] Later, Kuznetsov *et al.* developed a group of A-site substituted $Y_{1.8}M_{0.2}Ru_2O_{7-\delta}$ (M = Cu, Co, Ni, Fe, Y) with controllable oxygen vacancy concentration and demonstrated that the OER activity is highly correlated to oxygen vacancy concentration.[157] DFT calculations revealed that the enhanced activity along with increased oxygen vacancy concentration led to the lowered binding energy of the M–O band, which was scaling with the enthalpy of generation ($\Delta_f H_{oxide}$) of the respective MO_x species and the overlap between the M d orbitals and O 2p orbitals (Fig. 15h and i).

In addition to substitutional strategies for regulating electronic properties, the surface manipulation strategy is also proven to be an effective strategy for regulating the electronic properties of $A_2Ru_2O_7$ pyrochlore. Very recently, Liu *et al.* implanted MoO_x species on $Y_2Ru_2O_{7-\delta}$ to generate Mo–O–Ru micro-interfaces with accelerated electron transfer, which resulted in rearrangement of the Ru 4d orbital alignment and elimination of the bandgap.[158] In addition, the implanted MoO_x could not only compress the bond length of the Ru–O band and expand the Ru–O–Ru bond angle with moderate distortion of RuO6, but could also act as an electron receiver to induce more electronegative surfaces and prevent metal ions from dissolution, hence enhancing both OER activity and stability (Fig. 15j and k). Consequently, the obtained heterogeneous catalyst delivered an improved activity with an overpotential of 240 mV at 10 mA cm^{-2} and enhanced stability over 30 h relative to $Y_2Ru_2O_{7-\delta}$ (Fig. 15l).

As for perovskite-type ruthenates ($ARuO_3$), a thin film of $SrRuO_3$ OER catalyst with a very remarkable activity (1.33 V *vs.* RHE at 0.1 mA cm^{-2}) under alkaline conditions has been reported (Fig. 16a).[159] Nevertheless, the activity was completely degraded after only two cycles, which was due to not only the overoxidation of Ru under high voltages, but also the structure collapse of the perovskite starting at the Sr dissolution (Fig. 16a and b).[159,160] To overcome the lack of superior durability of Ru-related perovskites especially in acidic electrolytes, a series of B-site mixed $Sr_2(Ru_xIr_{1-x})O_4$ were prepared and proven to

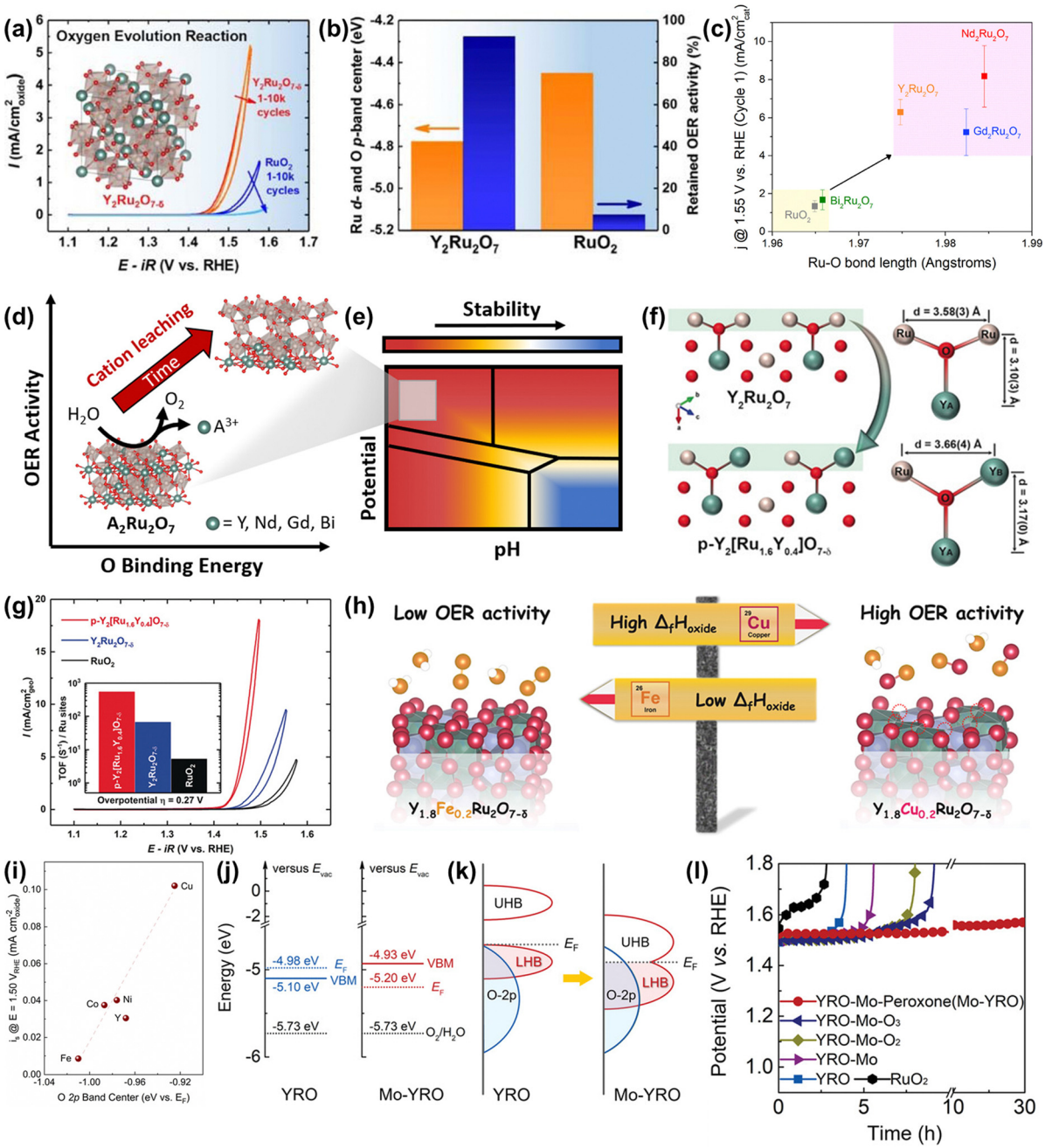

Fig. 15 (a) OER activities of $Y_2Ru_2O_{7-\delta}$ and RuO_2. (b) Comparison of the overlapped band center energy of Ru 4d and O 2p orbital and retained current density at 1.50 V for $Y_2Ru_2O_7$ and RuO_2, respectively.[154] (c) Current normalized by BET surface area for the first CV at 1.55 V *vs.* RHE as a function of Ru–O bond length determined from Ru K-edge EXAFS fits. (d) The relationships between OER activity and O binding energy of Ru-based pyrochlores. (e) Calculated Pourbaix diagrams of Ru-based pyrochlores.[146] (f) Illustrations of crystal structures of $Y_2Ru_2O_7$ and $Y_2[Ru_{1.6}Y_{0.4}]O_{7-\delta}$ pyrochlores, where Ru^{4+} is partially substituted by Y^{3+}.[155] (g) CVs and the corresponding TOFs (inset) of porous $Y_2[Ru_{1.6}Y_{0.4}]O_{7-\delta}$, $Y_2Ru_2O_{7-\delta}$, and RuO_2 electrocatalysts. (h) Scheme of the relationship between formation enthalpy and activity. (i) Correlation between the specific OER activity of $Y_{1.8}M_{0.2}Ru_2O_{7-\delta}$ estimated as current density at 1.50 V *vs* RHE and the O 2p band center position.[157] (j) Positions of VB and EF, together with E_{redox} of O_2/H_2O at pH = 0 (left for YRO, right for Mo-YRO). (k) Schematic evolution of band alignments after modification of YRO with MoO_x (LHB represents the lower Hubbard band and UHB represents the upper Hubbard band. (l) Chronopotentiometry curves for the stability tests of Mo-YRO, YRO, commercial RuO_2 and other YRO-Mo related materials at 10 mA cm^{-2}.[158]

display an optimal current density of 8.06 mA cm^{-2} at 1.55 V and good stability over 24 h at 10 mA cm^{-2} towards acidic OER (Fig. 16c), owing to the generation of enriched hydroxyl groups and the broadened Ru 4d band through the metal substitution.[161] In the same year, Xia *et al.* reported a B-site mixed $SrRu_{0.5}Ir_{0.5}O_3$ double perovskite with a strong electronic synergistic effect between Ir and Ru (Fig. 16d).[162] When used as an acidic OER catalyst, it showed a low overpotential of

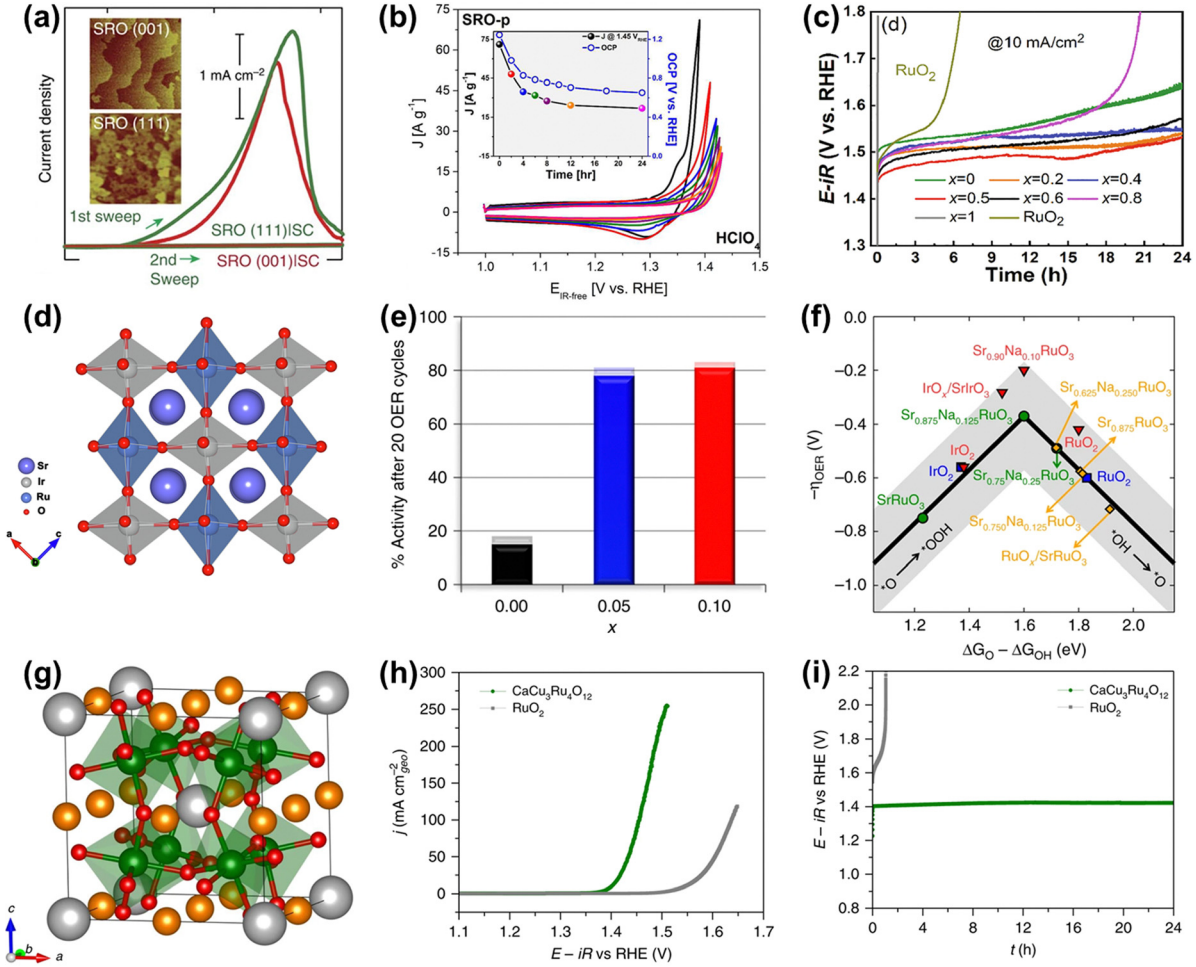

Fig. 16 (a) Current density measured (1st and 2nd sweep) at certain potentials of SRO(001) and SRO(111) side-connected with conducting paths from the top surface to the bottom substrate, denoted by SRO|SC.[159] (b) Chemical stability of SRO in contact with electrolytes in $HClO_4$.[160] (c) OER stability test of the SRIO-x series and reference RuO_2 electrocatalysts.[161] (d) Schematic illustration of the structures of $SrRu_{0.5}Ir_{0.5}O_3$.[162] (e) Percentage catalytic activity of $Sr_{1-x}Na_xRuO_3$ after 20 cycles with respect to the initial activity. (f) OER volcano-type activity plot.[163] (g) Crystal structure of $CaCu_3Ru_4O_{12}$. (h) Polarization curves of $CaCu_3Ru_4O_{12}$ and the commercial RuO_2 measured in O_2-saturated 0.5 M H_2SO_4 solution. (i) Chronopotentiometric measurements of $CaCu_3Ru_4O_{12}$ and the commercial RuO_2 at 10 mA cm^{-2}.[138]

185 mV at 10 mA cm^{-2} and stable stability for over 50 h. In addition to B-site substitution, A site-substituted ruthenium perovskite $Sr_{0.95}Na_{0.05}RuO_3$ was also found to be an enhanced acidic OER catalyst by Na^+ doping in the Sr^{2+} position.[163] Such perovskite catalysts showed an ultralow overpotential of only 120 mV at 0.5 mA cm^{-2} and improved structural stability (Fig. 16e), which was attributed to lower surface energy and higher dissolution potentials induced by Na-doping in the A-site (Fig. 16f). The HRTEM/digital diffraction pattern, STEM-HAADF micrographs with the line scans, and XPS results indicated that Na^+ doping suppressed the dissolution of Sr and Ru and increased the structural stability, not generating the different phases, such as RuO_x, during the OER. In general, metal substitutions can effectively regulate the electronic properties of perovskite-type ruthenates to greatly improve their catalytic performances. Furthermore, a quadruple perovskite oxide $CaCu_3Ru_4O_{12}$ (Fig. 16g) was reported to deliver an ultra-small overpotential of 171 mV at 10 mA cm^{-2} and much better stability compared to RuO_2 for acidic OER (Fig. 16h and i), which was due to a lower Ru 4d-band center in $CaCu_3Ru_4O_{12}$ relative to RuO_2.[138] These studies have indeed confirmed the role of electronic property tuning in achieving improved electrocatalytic performances and offered direction to the rational design of advanced Ru-based electrocatalysts.

Apart from the three types of Ru-based catalysts (Ru-based metal, oxides, and oxometallates) mentioned above, there are some other types of Ru-based catalysts, such as Ru chalcogenides ($RuTe_2$[164]) and Ru boride (RuB_2[165]), used for acidic OER. Although their stability is far from satisfaction, these advanced works are still great breakthroughs in the expansion of Ru-based acidic OER electrocatalysts.

4. Conclusions and perspectives

All in all, the four-electron transfer OER process on the surface of Ru-related catalysts is along with the redox of Ru or O sites,

in which the Ru element may dissolve under high overpotential and strong acidic conditions due to its severe overoxidation accompanied by the formation of the unstable and soluble RuO_4 species. Despite these drawbacks, Ru-based materials are still proven to be promising potential candidates for PEM anodic catalysts if the stability can be greatly enhanced. To date, Ru-based materials have been extensively studied to develop highly active and stable catalysts toward acidic OER. Thereinto, the effective and universal strategy to improve stability without sacrificing activity is to reduce the bulk oxygen diffusion rate and surface exchange kinetics of Ru-based catalysts whether following any reaction mechanisms. This review provides an overview of the recent advanced progress in Ru-related acidic OER catalysts, including metallic Ru, Ru-based oxides, and oxometallate-type ruthenates, and categorically summarizes the optimizing strategy to improve both stability and activity. Of note, most of the summarized strategies are applied to regulate the electronic structure to enhance the catalytic performances of Ru-based catalysts. Despite great progress, there remains a wide gap between experimental research and practical requirements. To further promote the development of Ru-based catalysts, many issues are still needed to be studied in depth.

Design of Ru-based materials

For the future development of highly active and stable Ru-related catalysts for acidic OER, heteroatom doping engineering on RuO_2 may be one of the promising and effective strategies. Of note, the previous studies involving heteroatom doped RuO_2 catalysts generally discuss the effect of doping engineering on electronic properties. However, the impact of structure engineering, such as specific microstructure, specific exposed facet, *etc.*, on Ru-based oxides is rarely considered. Therefore, developing heteroatom doped RuO_2 with a designed microstructure might be a resultful strategy. In addition, in view of the low reserves of Ru, atomically dispersed Ru atoms on an acid-stable non-noble metal oxide-based support (SA Ru/MO) is an ideal choice, which can not only reduce the consumption of noble metals but also construct unique geometric structures to enhance the stability of Ru-based catalysts. Nevertheless, mismatch in ionic radius, crystal structures, and electronegativity of different MOs makes the synthesis of SA Ru/MO significantly challenging. Consequently, new and effective synthetic methodologies to design advanced atomically dispersed Ru-based catalysts are needed to be explored. Furthermore, high-throughput theoretical calculations are recommended to screen advanced Ru-based catalysts for acidic OER.

Evaluation of the reaction process

Theoretical studies and various descriptors have been demonstrated to be effective tools for designing advanced Ru-based catalysts toward acidic OER. Of note, current theoretical calculations are usually based on simplified models without considering practical factors to simulate the complicated actual catalysts and reaction processes, which can only afford limited information to direct the development of Ru-based catalysts. Therefore, more actual factors should be taken into consideration, such as the actual catalyst model, surface thickness, pH, external electric field, the catalyst–electrolyte interface, *etc.*, thus uncovering a more realistic reaction process. In addition, current descriptors generally describe the bulk properties of Ru-based catalysts, being in inconformity with the viewpoint of actual reactions that occurred on the catalyst surface. Consequently, establishing a more precise descriptor should be based on the elaborate surface properties of Ru-based catalysts, and be further verified by abundant experimental evidence. More importantly, the actual active sites should be accurately identified, owing to the possible structure and/or phase reconstruction during the acidic OER process. To detailedly investigate the real active sites, some advanced *in situ*/operando XRD/XAS/Raman and isotope labeling techniques are needed to investigate the structural and electronic variation of Ru-based catalysts during the acidic OER process.

Evaluation of PEMWE

To promote the scalable application of PEMWE, the gap between laboratory studies and the typical industrial requirement (operating over 1 A cm^{-2} current density for over 10 years under 80 °C) should be plugged. Satisfactorily, Wen *et al.* recently prepared a Ni-stabilized RuO_2 (Ni-RuO_2) as the anode catalyst of PEMWE, displaying >1000 h stability at 200 mA cm^{-2}.[55] Further, Shi *et al.* constructed a $SnRuO_x$ solid solution oxide as an anode catalyst of PEMWE, showing a remarkable performance of working for 1300 h under 1 A cm^{-2} at 50 °C.[82] Although these designed catalysts do not meet the industrial requirement, they make the Ru-based catalysts a step closer to industrial application. More highly stable Ru-based catalysts with high activity are needed to be produced to satisfy the actual application in PEMWEs. Note that, the OER performance trends of catalysts might be different between the experimental method and industrial PEMWE. Moreover, the complex assembly process of the PEMWE cell may lead to certain deviations, which will result in some misleading information. Therefore, a standard protocol for not only evaluation (activity and stability) of anode catalysts in PEMWE under actual operating conditions but also PEMWE cell assembly should be established.

Conflicts of interest

The authors declare no competing interests.

Acknowledgements

We gratefully acknowledge the financial support from the Natural Science Foundation of Shandong Province of China (ZR2022QB100), Science Foundation of Qingdao University of Science and Technology (12030430010936), Taishan Scholar Program of Shandong Province, China (ts201712045) and Bk21Plus project of Korea.

References

1 Z. Seh, J. Kibsgaard and C. Dickens, *Science*, 2017, **355**, eaad4998.
2 H. Tian, A. Song, P. Zhang, K. Sun, J. Wang, B. Sun, Q. Fan, G. Shao, C. Chen, H. Liu, Y. Li and G. Wang, *Adv. Mater.*, 2023, **35**, 2210714.
3 Y. Xie, X. Chen, K. Sun, J. Zhang, W. Lai, H. Liu and G. Wang, *Angew. Chem., Int. Ed.*, 2023, **62**, e202301833.
4 L. She, G. Zhao, T. Ma, J. Chen, W. Sun and H. Pan, *Adv. Funct. Mater.*, 2022, **32**, 2108465.
5 Y. Jiao, Y. Zheng, M. Jaroniec and S. Z. Qiao, *Chem. Soc. Rev.*, 2015, **44**, 2060–2086.
6 C. Li, H. Jang, S. Liu, M. G. Kim, L. Hou, X. Liu and J. Cho, *Adv. Energy Mater.*, 2022, **12**, 2200029.
7 Y. Zhang, Z. Li, L. Hou and X. Liu, *Adv. Funct. Mater.*, 2023, **33**, 2213976.
8 G. S. Ogumerem and E. N. Pistikopoulos, *J. Process Contr.*, 2020, **91**, 37–49.
9 Q. Shi, C. Zhu, D. Du and Y. Lin, *Chem. Soc. Rev.*, 2019, **48**, 3181–3192.
10 R. LeRoy, *Int. J. Hydrog. Energy*, 1983, **8**, 401–417.
11 J. Russell, L. Nuttall and A. Fickett, *Am. Chem. Soc. Div. Fuel Chem. Prepr*, 1973, **18**, 24–40.
12 M. Carmo, D. L. Fritz, J. Mergel and D. Stolten, *Int. J. Hydrog. Energy*, 2013, **38**, 4901–4934.
13 F. Barbir, *Sol. Energy*, 2005, **78**, 661–669.
14 S. Slade, S. Campbell, T. Ralph and F. Walsh, *J. Electrochem. Soc.*, 2002, **149**, A1556.
15 T. Reier, H. N. Nong, D. Teschner, R. Schlögl and P. Strasser, *Adv. Energy Mater.*, 2017, **7**, 1601275.
16 L. An, C. Wei, M. Lu, H. Liu, Y. Chen, G. G. Scherer, A. C. Fisher, P. Xi, Z. J. Xu and C. H. Yan, *Adv. Mater.*, 2021, **33**, 2006328.
17 Q. Wang, Y. Cheng, H. B. Tao, Y. Liu, X. Ma, D. S. Li, H. B. Yang and B. Liu, *Angew. Chem., Int. Ed.*, 2023, **62**, e202216645.
18 N.-T. Suen, S.-F. Hung, Q. Quan, N. Zhang, Y.-J. Xu and H. M. Chen, *Chem. Soc. Rev.*, 2017, **46**, 337–365.
19 Q. Qin, H. Jang, L. Chen, G. Nam, X. Liu and J. Cho, *Adv. Energy Mater.*, 2018, **8**, 1801478.
20 L. Hou, H. Jang, H. Liu, Z. Li, M. G. Kim, Q. Qin and X. Liu, *ACS Sustain. Chem. Eng.*, 2022, **10**, 15950–15957.
21 H. Sun, X. Xu, H. Kim, W. Jung, W. Zhou and Z. Shao, *Energy Environ. Mater.*, 2022, **0**, e12441.
22 C. Li, H. Jang, M. G. Kim, L. Hou, X. Liu and J. Cho, *Appl. Catal., B*, 2022, **307**, 121204.
23 G. Li, H. Jang, S. Liu, Z. Li, M. G. Kim, Q. Qin, X. Liu and J. Cho, *Nat. Commun.*, 2022, **13**, 1270.
24 F.-Y. Chen, Z.-Y. Wu, Z. Adler and H. Wang, *Joule*, 2021, **5**, 1704–1731.
25 Y. Wang, Z. Li, L. Hou, Y. Wang, L. Zhang, T. Wang, H. Liu, S. Liu, Q. Qin and X. Liu, *ACS Appl. Mater. Interfaces*, 2023, **15**, 14282–14290.
26 H. Sun and W. Jung, *J. Mater. Chem. A*, 2021, **9**, 15506–15521.
27 Q. Qin, H. Jang, Y. Wang, L. Zhang, Z. Li, M. G. Kim, S. Liu, X. Liu and J. Cho, *Adv. Energy Mater.*, 2021, **11**, 2003561.
28 L. Li, X. Cao, J. Huo, J. Qu, W. Chen, C. Liu, Y. Zhao, H. Liu and G. Wang, *J. Energy Chem.*, 2023, **76**, 195–213.
29 A. M. Patel, J. K. Nørskov, K. A. Persson and J. H. Montoya, *Phys. Chem. Chem. Phys.*, 2019, **21**, 25323–25327.
30 Z. Chen, L. Guo, L. Pan, T. Yan, Z. He, Y. Li, C. Shi, Z. F. Huang, X. Zhang and J. J. Zou, *Adv. Energy Mater.*, 2022, **12**, 2103670.
31 L. Fu, F. Yang, G. Cheng and W. Luo, *Nanoscale*, 2018, **10**, 1892–1897.
32 Z. Fan, Y. Ji, Q. Shao, S. Geng, W. Zhu, Y. Liu, F. Liao, Z. Hu, Y.-C. Chang and C.-W. Pao, *Joule*, 2021, **5**, 3221–3234.
33 L. Yang, L. Shi, H. Chen, X. Liang, B. Tian, K. Zhang, Y. Zou and X. Zou, *Adv. Mater.*, 2022, 2208539.
34 F. Liao, K. Yin, Y. Ji, W. Zhu, Z. Fan, Y. Li, J. Zhong, M. Shao, Z. Kang and Q. Shao, *Nat. Commun.*, 2023, **14**, 1248.
35 P. C. Vesborg and T. F. Jaramillo, *RSC Adv.*, 2012, **2**, 7933–7947.
36 A. Hauch, R. Küngas, P. Blennow, A. B. Hansen, J. B. Hansen, B. V. Mathiesen and M. B. Mogensen, *Science*, 2020, **370**, eaba6118.
37 R. M. Bullock, J. G. Chen, L. Gagliardi, P. J. Chirik, O. K. Farha, C. H. Hendon, C. W. Jones, J. A. Keith, J. Klosin and S. D. Minteer, *Science*, 2020, **369**, eabc3183.
38 J. Ying, J.-B. Chen, Y.-X. Xiao, S. I. C. de Torresi, K. I. Ozoemena and X.-Y. Yang, *J. Mater. Chem. A*, 2023, **11**, 1634–1650.
39 X. Cao, J. Huo, L. Li, J. Qu, Y. Zhao, W. Chen, C. Liu, H. Liu and G. Wang, *Adv. Energy Mater.*, 2022, **12**, 2202119.
40 J. Shan, Y. Zheng, B. Shi, K. Davey and S.-Z. Qiao, *ACS Energy Lett.*, 2019, **4**, 2719–2730.
41 M. Zhao, Z. Chen, Z. Lyu, Z. D. Hood, M. Xie, M. Vara, M. Chi and Y. Xia, *J. Am. Chem. Soc.*, 2019, **141**, 7028–7036.
42 J. Shan, T. Ling, K. Davey, Y. Zheng and S. Z. Qiao, *Adv. Mater.*, 2019, **31**, 1900510.
43 Q. Zhang, K. Kusada, D. Wu, N. Ogiwara, T. Yamamoto, T. Toriyama, S. Matsumura, S. Kawaguchi, Y. Kubota and T. Honma, *Chem. Sci.*, 2019, **10**, 5133–5137.
44 Y. Yao, S. Hu, W. Chen, Z.-Q. Huang, W. Wei, T. Yao, R. Liu, K. Zang, X. Wang and G. Wu, *Nat. Catal.*, 2019, **2**, 304–313.
45 Y. Qin, T. Yu, S. Deng, X.-Y. Zhou, D. Lin, Q. Zhang, Z. Jin, D. Zhang, Y.-B. He and H.-J. Qiu, *Nat. Commun.*, 2022, **13**, 3784.
46 J. Yu, Q. He, G. Yang, W. Zhou, Z. Shao and M. Ni, *ACS Catal.*, 2019, **9**, 9973–10011.
47 R. Walker, M. Bailes and L. Peter, *Electrochim. Acta*, 1998, **44**, 1289–1294.
48 A. Izgorodin, O. Winther-Jensen and D. R. MacFarlane, *Aust. J. Chem.*, 2012, **65**, 638–642.
49 L. Zhang, H. Jang, H. Liu, M. G. Kim, D. Yang, S. Liu, X. Liu and J. Cho, *Angew. Chem., Int. Ed.*, 2021, **133**, 18969–18977.

50 C.-J. Chang, Y.-C. Chu, H.-Y. Yan, Y.-F. Liao and H. M. Chen, *Dalton Trans.*, 2019, **48**, 7122–7129.
51 H. Jin, X. Liu, P. An, C. Tang, H. Yu, Q. Zhang, H.-J. Peng, L. Gu, Y. Zheng and T. Song, *Nat. Commun.*, 2023, **14**, 354.
52 H. Liu, Z. Zhang, J. Fang, M. Li, M. G. Sendeku, X. Wang, H. Wu, Y. Li, J. Ge and Z. Zhuang, *Joule*, 2023, **7**, 558–573.
53 Y. Wen, C. Liu, R. Huang, H. Zhang, X. Li, F. P. García de Arquer, Z. Liu, Y. Li and B. Zhang, *Nat. Commun.*, 2022, **13**, 4871.
54 N. Yao, H. Jia, J. Zhu, Z. Shi, H. Cong, J. Ge and W. Luo, *Chem*, 2023, **9**, 1–15.
55 Z.-Y. Wu, F.-Y. Chen, B. Li, S.-W. Yu, Y. Z. Finfrock, D. M. Meira, Q.-Q. Yan, P. Zhu, M.-X. Chen and T.-W. Song, *Nat. Mater.*, 2023, **22**, 100–108.
56 Y. Wang, R. Yang, Y. Ding, B. Zhang, H. Li, B. Bai, M. Li, Y. Cui, J. Xiao and Z.-S. Wu, *Nat. Commun.*, 2023, **14**, 1412.
57 R. R. Rao, M. J. Kolb, L. Giordano, A. F. Pedersen, Y. Katayama, J. Hwang, A. Mehta, H. You, J. R. Lunger and H. Zhou, *Nat. Catal.*, 2020, **3**, 516–525.
58 K. A. Stoerzinger, O. Diaz-Morales, M. Kolb, R. R. Rao, R. Frydendal, L. Qiao, X. R. Wang, N. B. Halck, J. Rossmeisl and H. A. Hansen, *ACS Energy Lett.*, 2017, **2**, 876–881.
59 X. Peng, S. Zhao, Y. Mi, L. Han, X. Liu, D. Qi, J. Sun, Y. Liu, H. Bao and L. Zhuo, *Small*, 2020, **16**, 2002888.
60 L. Qiu, G. Zheng, Y. He, L. Lei and X. Zhang, *Chem. Eng. J.*, 2021, **409**, 128155.
61 J. Rossmeisl, Z.-W. Qu, H. Zhu, G.-J. Kroes and J. K. Nørskov, *J. Electroanal. Chem.*, 2007, **607**, 83–89.
62 I. C. Man, H. Y. Su, F. Calle-Vallejo, H. A. Hansen, J. I. Martínez, N. G. Inoglu, J. Kitchin, T. F. Jaramillo, J. K. Nørskov and J. Rossmeisl, *ChemCatChem*, 2011, **3**, 1159–1165.
63 E. A. Paoli, F. Masini, R. Frydendal, D. Deiana, C. Schlaup, M. Malizia, T. W. Hansen, S. Horch, I. E. Stephens and I. Chorkendorff, *Chem. Sci.*, 2015, **6**, 190–196.
64 J. Lee, A. Kumar, T. Yang, X. Liu, A. R. Jadhav, G. H. Park, Y. Hwang, J. Yu, C. T. Nguyen and Y. Liu, *Energy Environ. Sci.*, 2020, **13**, 5152–5164.
65 N. B. Halck, V. Petrykin, P. Krtil and J. Rossmeisl, *Phys. Chem. Chem. Phys.*, 2014, **16**, 13682–13688.
66 Y.-H. Fang and Z.-P. Liu, *J. Am. Chem. Soc.*, 2010, **132**, 18214–18222.
67 D. Chen, Y.-H. Fang and Z.-P. Liu, *Phys. Chem. Chem. Phys.*, 2012, **14**, 16612–16617.
68 C. Wei, Z. Feng, G. G. Scherer, J. Barber, Y. Shao-Horn and Z. J. Xu, *Adv. Mater.*, 2017, **29**, 1606800.
69 M. J. Craig and M. Garcia-Melchor, *Curr. Opin. Electrochem.*, 2022, 101044.
70 X. Cheng, E. Fabbri, Y. Yamashita, I. E. Castelli, B. Kim, M. Uchida, R. Haumont, I. Puente-Orench and T. J. Schmidt, *ACS Catal.*, 2018, **8**, 9567–9578.
71 J. K. Nørskov, F. Abild-Pedersen, F. Studt and T. Bligaard, *Proc. Natl. Acad. Sci. U. S. A.*, 2011, **108**, 937–943.
72 Z.-J. Zhao, S. Liu, S. Zha, D. Cheng, F. Studt, G. Henkelman and J. Gong, *Nat. Rev. Mater.*, 2019, **4**, 792–804.
73 J. Li, *Nanomicro Lett.*, 2022, **14**, 112.
74 Y. Hu, D. Huang, J. Zhang, Y. Huang, M. S. J. T. Balogun and Y. Tong, *ChemCatChem*, 2019, **11**, 6051–6060.
75 D. Luo, B. Yang, Z. Mei, Q. Kang, G. Chen, X. Liu and N. Zhang, *ACS Appl. Mater. Interfaces*, 2022, **14**, 52857–52867.
76 K. Yang, P. Xu, Z. Lin, Y. Yang, P. Jiang, C. Wang, S. Liu, S. Gong, L. Hu and Q. Chen, *Small*, 2018, **14**, 1803009.
77 W. T. Hong, M. Risch, K. A. Stoerzinger, A. Grimaud, J. Suntivich and Y. Shao-Horn, *Energy Environ. Sci.*, 2015, **8**, 1404–1427.
78 S. Liu, Y. Chang, N. He, S. Zhu, L. Wang and X. Liu, *ACS Appl. Mater. Interfaces*, 2023, **15**, 20563–20570.
79 Y. Matsumoto, H. Yoneyama and H. Tamura, *J. Electroanal. Chem. Interfacial Electrochem.*, 1977, **79**, 319–326.
80 J. Hwang, R. R. Rao, L. Giordano, Y. Katayama, Y. Yu and Y. Shao-Horn, *Science*, 2017, **358**, 751–756.
81 H. B. Tao, L. Fang, J. Chen, H. B. Yang, J. Gao, J. Miao, S. Chen and B. Liu, *J. Am. Chem. Soc.*, 2016, **138**, 9978–9985.
82 Z. Shi, J. Li, Y. Wang, S. Liu, J. Zhu, J. Yang, X. Wang, J. Ni, Z. Jiang and L. Zhang, *Nat. Commun.*, 2023, **14**, 843.
83 T. Reier, M. Oezaslan, P. Strasser and A. Catal, *P. Grote, A. Savan, BR Shrestha, S. Merzlikin, B. Breitbach, A. Ludwig, Catal. Today*, 2016, **262**, 170–180.
84 E. Paoli, F. Masini, R. Frydendal, D. Deiana, C. Schlaup, M. Malizia, T. Hansen, S. Horch, I. Stephens and I. Chorkendorff, *Chem. Sci.*, 2015, **6**, 190–196.
85 R. Kötz, H. Lewerenz and S. Stucki, *J. Electrochem. Soc.*, 1983, **130**, 825.
86 R. Kötz, S. Stucki, D. Scherson and D. Kolb, *J. Electroanal. Chem. Interfacial Electrochem.*, 1984, **172**, 211–219.
87 K. Klyukin, A. Zagalskaya and V. Alexandrov, *J. Phys. Chem. C*, 2019, **123**, 22151–22157.
88 S. Cherevko, *Curr. Opin. Electrochem.*, 2018, **8**, 118–125.
89 S. Cherevko, A. R. Zeradjanin, A. A. Topalov, N. Kulyk, I. Katsounaros and K. J. Mayrhofer, *ChemCatChem*, 2014, **6**, 2219–2223.
90 J. S. Yoo, X. Rong, Y. Liu and A. M. Kolpak, *ACS Catal.*, 2018, **8**, 4628–4636.
91 A. Grimaud, O. Diaz-Morales, B. Han, W. T. Hong, Y.-L. Lee, L. Giordano, K. A. Stoerzinger, M. T. Koper and Y. Shao-Horn, *Nat. Chem.*, 2017, **9**, 457–465.
92 X. Wang, H. Zhong, S. Xi, W. S. V. Lee and J. Xue, *Adv. Mater.*, 2022, **34**, 2107956.
93 T. Bligaard, J. K. Nørskov, S. Dahl, J. Matthiesen, C. H. Christensen and J. Sehested, *J. Catal.*, 2004, **224**, 206–217.
94 P. Adiga, W. Nunn, C. Wong, A. K. Manjeshwar, S. Nair, B. Jalan and K. A. Stoerzinger, *Mater. Today Energy*, 2022, **28**, 101087.
95 S. Geiger, O. Kasian, M. Ledendecker, E. Pizzutilo, A. M. Mingers, W. T. Fu, O. Diaz-Morales, Z. Li, T. Oellers and L. Fruchter, *Nat. Catal.*, 2018, **1**, 508–515.
96 C. Roy, R. R. Rao, K. A. Stoerzinger, J. Hwang, J. Rossmeisl, I. Chorkendorff, Y. Shao-Horn and I. E. Stephens, *ACS Energy Lett.*, 2018, **3**, 2045–2051.

97 Y. Tian, S. Wang, E. Velasco, Y. Yang, L. Cao, L. Zhang, X. Li, Y. Lin, Q. Zhang and L. Chen, *iScience*, 2020, **23**, 100756.
98 M. T. Koper, *Chem. Sci.*, 2013, **4**, 2710–2723.
99 C. Lin, J.-L. Li, X. Li, S. Yang, W. Luo, Y. Zhang, S.-H. Kim, D.-H. Kim, S. S. Shinde and Y.-F. Li, *Nat. Catal.*, 2021, **4**, 1012–1023.
100 A. R. Poerwoprajitno, L. Gloag, T. M. Benedetti, S. Cheong, J. Watt, D. L. Huber, J. J. Gooding and R. D. Tilley, *Small*, 2019, **15**, 1804577.
101 Z. Xia and S. Guo, *Chem. Soc. Rev.*, 2019, **48**, 3265–3278.
102 X. Yang, Y. Wang, X. Tong and N. Yang, *Adv. Energy Mater.*, 2022, **12**, 2102261.
103 J.-Q. Wang, C. Xi, M. Wang, L. Shang, J. Mao, C.-K. Dong, H. Liu, S. A. Kulinich and X.-W. Du, *ACS Catal.*, 2020, **10**, 12575–12581.
104 R. Forgie, G. Bugosh, K. Neyerlin, Z. Liu and P. Strasser, *Electrochem. Solid-State Lett.*, 2010, **13**, B36.
105 N. Danilovic, R. Subbaraman, K. C. Chang, S. H. Chang, Y. Kang, J. Snyder, A. P. Paulikas, D. Strmcnik, Y. T. Kim and D. Myers, *Angew. Chem., Int. Ed.*, 2014, **53**, 14016–14021.
106 Y. Jiang, Y. Mao, Y. Jiang, H. Liu, W. Shen, M. Li and R. He, *Chem. Eng. J.*, 2022, **450**, 137909.
107 L. An, F. Yang, C. Fu, X. Cai, S. Shen, G. Xia, J. Li, Y. Du, L. Luo and J. Zhang, *Adv. Funct. Mater.*, 2022, **32**, 2200131.
108 Q. Yao, B. Huang, N. Zhang, M. Sun, Q. Shao and X. Huang, *Angew. Chem., Int. Ed.*, 2019, **131**, 14121–14126.
109 L. Li, L. Bu, B. Huang, P. Wang, C. Shen, S. Bai, T. S. Chan, Q. Shao, Z. Hu and X. Huang, *Adv. Mater.*, 2021, **33**, 2105308.
110 J. Xu, J. Li, Z. Lian, A. Araujo, Y. Li, B. Wei, Z. Yu, O. Bondarchuk, I. Amorim and V. Tileli, *ACS Catal.*, 2021, **11**, 3402–3413.
111 T. Zhu, S. Liu, B. Huang, Q. Shao, M. Wang, F. Li, X. Tan, Y. Pi, S.-C. Weng and B. Huang, *Energy Environ. Sci.*, 2021, **14**, 3194–3202.
112 J. Zhu, Y. Guo, F. Liu, H. Xu, L. Gong, W. Shi, D. Chen, P. Wang, Y. Yang and C. Zhang, *Angew. Chem., Int. Ed.*, 2021, **133**, 12436–12442.
113 J. Shan, C. Guo, Y. Zhu, S. Chen, L. Song, M. Jaroniec, Y. Zheng and S.-Z. Qiao, *Chem*, 2019, **5**, 445–459.
114 D. Chen, R. Yu, D. Wu, H. Zhao, P. Wang, J. Zhu, P. Ji, Z. Pu, L. Chen and J. Yu, *Nano Energy*, 2022, **100**, 107445.
115 X.-F. Yang, A. Wang, B. Qiao, J. Li, J. Liu and T. Zhang, *Acc. Chem. Res.*, 2013, **46**, 1740–1748.
116 R. Lang, X. Du, Y. Huang, X. Jiang, Q. Zhang, Y. Guo, K. Liu, B. Qiao, A. Wang and T. Zhang, *Chem. Rev.*, 2020, **120**, 11986–12043.
117 Y. Chen, S. Ji, C. Chen, Q. Peng, D. Wang and Y. Li, *Joule*, 2018, **2**, 1242–1264.
118 L. Cao, Q. Luo, J. Chen, L. Wang, Y. Lin, H. Wang, X. Liu, X. Shen, W. Zhang and W. Liu, *Nat. Commun.*, 2019, **10**, 4849.
119 C. Rong, X. Shen, Y. Wang, L. Thomsen, T. Zhao, Y. Li, X. Lu, R. Amal and C. Zhao, *Adv. Mater.*, 2022, **34**, 2110103.
120 Z. Wang, Y.-R. Zheng, I. Chorkendorff and J. K. Nørskov, *ACS Energy Lett.*, 2020, **5**, 2905–2908.
121 A. Li, H. Ooka, N. Bonnet, T. Hayashi, Y. Sun, Q. Jiang, C. Li, H. Han and R. Nakamura, *Angew. Chem., Int. Ed.*, 2019, **131**, 5108–5112.
122 Z. L. Zhao, Q. Wang, X. Huang, Q. Feng, S. Gu, Z. Zhang, H. Xu, L. Zeng, M. Gu and H. Li, *Energy Environ. Sci.*, 2020, **13**, 5143–5151.
123 R. Ge, L. Li, J. Su, Y. Lin, Z. Tian and L. Chen, *Adv. Energy Mater.*, 2019, **9**, 1901313.
124 S. C. Sun, H. Jiang, Z. Y. Chen, Q. Chen, M. Y. Ma, L. Zhen, B. Song and C. Y. Xu, *Angew. Chem., Int. Ed.*, 2022, **134**, e202202519.
125 Y. Li, W. Wang, M. Cheng, Y. Feng, X. Han, Q. Qian, Y. Zhu and G. Zhang, *Adv. Mater.*, 2023, 2206351.
126 X. Cui, P. Ren, C. Ma, J. Zhao, R. Chen, S. Chen, N. P. Rajan, H. Li, L. Yu and Z. Tian, *Adv. Mater.*, 2020, **32**, 1908126.
127 X. Wang, X. Wan, X. Qin, C. Chen, X. Qian, Y. Guo, Q. Xu, W.-B. Cai, H. Yang and K. Jiang, *ACS Catal.*, 2022, **12**, 9437–9445.
128 S. Niu, X.-P. Kong, S. Li, Y. Zhang, J. Wu, W. Zhao and P. Xu, *Appl. Catal., B*, 2021, **297**, 120442.
129 T. Kwon, H. Yang, M. Jun, T. Kim, J. Joo, J. Kim, H. Baik, J. Y. Kim and K. Lee, *J. Mater. Chem. A*, 2021, **9**, 14352–14362.
130 J. F. Godinez-Salomon, F. Ospina-Acevedo, L. A. Albiter, K. O. Bailey, Z. G. Naymik, R. Mendoza-Cruz, P. B. Balbuena and C. P. Rhodes, *ACS Appl. Nano Mater.*, 2022, **5**, 11752–11775.
131 Y. Lin, Z. Tian, L. Zhang, J. Ma, Z. Jiang, B. J. Deibert, R. Ge and L. Chen, *Nat. Commun.*, 2019, **10**, 162.
132 K. Wang, Y. Wang, B. Yang, Z. Li, X. Qin, Q. Zhang, L. Lei, M. Qiu, G. Wu and Y. Hou, *Energy Environ. Sci.*, 2022, **15**, 2356–2365.
133 Y. Xue, J. Fang, X. Wang, Z. Xu, Y. Zhang, Q. Lv, M. Liu, W. Zhu and Z. Zhuang, *Adv. Funct. Mater.*, 2021, **31**, 2101405.
134 K. Shah, R. Dai, M. Mateen, Z. Hassan, Z. Zhuang, C. Liu, M. Israr, W. C. Cheong, B. Hu and R. Tu, *Angew. Chem., Int. Ed.*, 2022, **134**, e202114951.
135 J. Su, R. Ge, K. Jiang, Y. Dong, F. Hao, Z. Tian, G. Chen and L. Chen, *Adv. Mater.*, 2018, **30**, 1801351.
136 L. Hou, Z. Li, H. Jang, Y. Wang, X. Cui, X. Gu, M. G. Kim, L. Feng, S. Liu and X. Liu, *Adv. Energy Mater.*, 2023, 2300177.
137 Z. Li, S. Wang, Y. Tian, B. Li, H. Jun Yan, S. Zhang, Z. Liu, Q. Zhang, Y. Lin and L. Chen, *Chem. Commun.*, 2020, **56**, 1749–1752.
138 X. Miao, L. Zhang, L. Wu, Z. Hu, L. Shi and S. Zhou, *Nat. Commun.*, 2019, **10**, 3809.
139 Y. Wen, P. Chen, L. Wang, S. Li, Z. Wang, J. Abed, X. Mao, Y. Min, C. T. Dinh and P. D. Luna, *J. Am. Chem. Soc.*, 2021, **143**, 6482–6490.
140 H. Jin, S. Choi, G. J. Bang, T. Kwon, H. S. Kim, S. J. Lee, Y. Hong, D. W. Lee, H. S. Park and H. Baik, *Energy Environ. Sci.*, 2022, **15**, 1119–1130.

141 J. He, X. Zhou, P. Xu and J. Sun, *Adv. Energy Mater.*, 2021, **11**, 2102883.
142 R. Huang, Y. Wen, H. Peng and B. Zhang, *Chin. J. Catal.*, 2022, **43**, 130–138.
143 Y. Wu, R. Yao, Q. Zhao, J. Li and G. Liu, *Chem. Eng. J.*, 2022, **439**, 135699.
144 J. He, W. Li, P. Xu and J. Sun, *Appl. Catal., B*, 2021, **298**, 120528.
145 N. Han, S. Feng, Y. Liang, J. Wang, W. Zhang, X. Guo, Q. Ma, Q. Liu, W. Guo and Z. Zhou, *Adv. Funct. Mater.*, 2023, 2208399.
146 M. A. Hubert, A. M. Patel, A. Gallo, Y. Liu, E. Valle, M. Ben-Naim, J. Sanchez, D. Sokaras, R. Sinclair and J. K. Nørskov, *ACS Catal.*, 2020, **10**, 12182–12196.
147 J. He, W. Chen, H. Gao, Y. Chen, L. Zhou, Y. Zou, R. Chen, L. Tao, X. Lu and S. Wang, *Chem. Catal.*, 2022, **2**, 578–594.
148 J. Wang, C. Cheng, Q. Yuan, H. Yang, F. Meng, Q. Zhang, L. Gu, J. Cao, L. Li and S.-C. Haw, *Chem*, 2022, **8**, 1673–1687.
149 C. Liu, B. Sheng, Q. Zhou, D. Cao, H. Ding, S. Chen, P. Zhang, Y. Xia, X. Wu and L. Song, *Nano Res.*, 2022, **15**, 7008–7015.
150 Q. Yao, Z. Yu, Y.-H. Chu, Y.-H. Lai, T.-S. Chan, Y. Xu, Q. Shao and X. Huang, *Nano Res.*, 2022, **15**, 3964–3970.
151 K. Huang, C. Lin, G. Yu, P. Du, X. Xie, X. He, Z. Zheng, N. Sun, H. Tang and X. Li, *Adv. Funct. Mater.*, 2023, **33**, 2211102.
152 C. Liu, Y. Jiang, T. Wang, Q. Li and Y. Liu, *Adv. Sci.*, 2023, **10**, 2207429.
153 J. Wang, H. Yang, F. Li, L. Li, J. Wu, S. Liu, T. Cheng, Y. Xu, Q. Shao and X. Huang, *Sci. Adv.*, 2022, **8**, eabl9271.
154 J. Kim, P.-C. Shih, K.-C. Tsao, Y.-T. Pan, X. Yin, C.-J. Sun and H. Yang, *J. Am. Chem. Soc.*, 2017, **139**, 12076–12083.
155 J. Kim, P. C. Shih, Y. Qin, Z. Al-Bardan, C. J. Sun and H. Yang, *Angew. Chem., Int. Ed.*, 2018, **130**, 14073–14077.
156 Q. Feng, Q. Wang, Z. Zhang, Y. Xiong, H. Li, Y. Yao, X.-Z. Yuan, M. C. Williams, M. Gu and H. Chen, *Appl. Catal., B*, 2019, **244**, 494–501.
157 D. A. Kuznetsov, M. A. Naeem, P. V. Kumar, P. M. Abdala, A. Fedorov and C. R. Müller, *J. Am. Chem. Soc.*, 2020, **142**, 7883–7888.
158 T. Liu, H. Guo, Y. Chen, Z. Zhang and F. Wang, *Small*, 2023, 2206698.
159 S. H. Chang, N. Danilovic, K.-C. Chang, R. Subbaraman, A. P. Paulikas, D. D. Fong, M. J. Highland, P. M. Baldo, V. R. Stamenkovic and J. W. Freeland, *Nat. Commun.*, 2014, **5**, 4191.
160 B.-J. Kim, D. F. Abbott, X. Cheng, E. Fabbri, M. Nachtegaal, F. Bozza, I. E. Castelli, D. Lebedev, R. Schäublin and C. Coperet, *ACS Catal.*, 2017, **7**, 3245–3256.
161 F. Wang, C. Zhang and H. Yang, *J. Energy Chem.*, 2022, **70**, 623–629.
162 T. Xia, C. Liu, Y. Lu, W. Jiang, H. Li, Y. Ma, Y. Wu and G. Che, *Appl. Surf. Sci.*, 2022, **605**, 154727.
163 M. Retuerto, L. Pascual, F. Calle-Vallejo, P. Ferrer, D. Gianolio, A. G. Pereira, Á. García, J. Torrero, M. T. Fernández-Díaz and P. Bencok, *Nat. Commun.*, 2019, **10**, 2041.
164 J. Wang, L. Han, B. Huang, Q. Shao, H. L. Xin and X. Huang, *Nat. Commun.*, 2019, **10**, 5692.
165 D. Chen, T. Liu, P. Wang, J. Zhao, C. Zhang, R. Cheng, W. Li, P. Ji, Z. Pu and S. Mu, *ACS Energy Lett.*, 2020, **5**, 2909–2915.